JGR Atmospheres

RESEARCH ARTICLE
10.1029/2022JD037724

# Dust Settling From Turbulent Layers in the Free Troposphere: Implications for the Saharan Air Layer

**Rodrigo Rodakoviski[1], Jasper Kok[1], and Marcelo Chamecki[1]**

[1]Department of Atmospheric & Oceanic Sciences, University of California in Los Angeles, Los Angeles, CA, USA

**Key Points:**

- Turbulent mixing is capable of at most doubling the atmospheric lifetime of coarse aerosols in elevated layers
- Airborne lifetime of particles depends only on the relative strength of gravitational settling and turbulent mixing
- Dust asphericity and free tropospheric mixing help explain the transport of super coarse Saharan dust to the Caribbean

**Supporting Information:**

Supporting Information may be found in the online version of this article.

**Correspondence to:**

M. Chamecki,
chamecki@ucla.edu

**Citation:**

Rodakoviski, R., Kok, J., & Chamecki, M. (2023). Dust settling from turbulent layers in the free troposphere: Implications for the Saharan Air Layer. *Journal of Geophysical Research: Atmospheres*, *128*, e2022JD037724. https://doi.org/10.1029/2022JD037724

Received 24 AUG 2022
Accepted 27 FEB 2023

**Abstract** Desert dust accounts for a substantial fraction of the total atmospheric aerosol loading. It produces important impacts on the Earth system due to its nutrient content and interactions with radiation and clouds. However, current climate models greatly underestimate its airborne lifetime and transport. For instance, super coarse Saharan dust particles (with diameters greater than 10 μm) have repeatedly been detected in the Americas, but models fail to reproduce their transatlantic transport. In this study, we investigated the extent to which vertical turbulent mixing in the Saharan Air Layer (SAL) is capable of delaying particle deposition. We developed a theory based on the solution to a one-dimensional dust mass balance and validated our results using large-eddy simulation (LES) of a turbulent shear layer. We found that eddy motion can increase the lifetime of suspended particles by up to a factor of 2 when compared with laminar flows. Moreover, we found that the increase in a lifetime can be reliably estimated solely as a function of the particle Peclet number (the ratio of the mixing timescale to the settling timescale). By considering both the effects of turbulent mixing and dust asphericity, we explained to a large extent the presence of super coarse Saharan dust in the Caribbean observed during the Saharan Aerosol Long-Range Transport and Aerosol-Cloud-Interaction Experiment (SALTRACE) field campaign. The theory for the lifetime of coarse particles in turbulent flows developed in this study is also expected to be applicable in other similar geophysical problems, such as phytoplankton sinking in the ocean mixed layer.

**Plain Language Summary** Dust emitted from desert surfaces on Earth impacts climate and weather by affecting cloud formation and interacting with solar and terrestrial radiation. It also carries important nutrients that feed land and ocean ecosystems. Therefore, it is important to accurately predict for how long these particles remain suspended in the atmosphere. However, current models underestimate this time and the associated horizontal transport. For example, it is still not well understood how super coarse dust particles (which deposit faster than smaller particles) are able to move from the Sahara desert to the Americas. Our study tested the hypothesis that vertical mixing caused by turbulence in the upper atmosphere (above about 2 km from the ground) is one of the mechanisms responsible for that phenomenon. Using the principle of mass conservation, as well as computer simulations, we found that turbulence can even double the period of time that dust remains suspended in the atmosphere. When also factoring in the irregular shape of dust particles, which decreases their deposition speeds, our theory was able to explain to a great extent observations of super coarse Saharan particles in the Caribbean. This suggests that turbulence is a key mechanism by which dust gets transported over long distances.

## 1. Introduction

Desert dust accounts for about 70% of the global atmospheric aerosol mass (Tsigaridis et al., 2006). It carries key micronutrients to terrestrial and oceanic ecosystems (e.g., Chien et al., 2016; Yu et al., 2015) and potentially affects human activity by degrading visibility and human health (Middleton, 2017). Moreover, its interactions with radiation (Kok et al., 2017; Otto et al., 2007) and clouds (DeMott et al., 2003; Twohy et al., 2009) cause airborne dust to influence weather and climate significantly. In fact, the greatest uncertainty in Earth's energy budget estimates is still due to the contribution of aerosols and clouds (IPCC, 2021).

Despite its importance, and while it has been known that dust in the atmosphere deposits slower than predicted by Stokes' settling speed or simulated in large-scale models (e.g., Adebiyi & Kok, 2020; Kim et al., 2014; Maring et al., 2003), the processes responsible for keeping such particles suspended in the atmosphere for so long, especially those in the coarse and super coarse modes (i.e., those with volume-equivalent diameters greater than 5 and 10 μm, respectively), are still not fully understood. In fact, Adebiyi and Kok (2020) estimated that the global load

of coarse dust is actually four times greater than climate models currently simulate. This missing dust causes a net warming of the climate system due to the absorption of solar and terrestrial radiation.

Perhaps the most well-known dust transport pathway in the atmosphere is the so-called Saharan Air Layer (SAL), a hot, dry, dust-laden air layer originating from North Africa and traveling across the tropical North Atlantic toward the Americas over the course of about 5 days (Carlson & Prospero, 1972). The SAL is not directly in contact with Earth's surface; it rather is situated above the cooler, moister trade-wind layer, separated from it by a temperature inversion which is typically located at about 1.5-km altitude off the west coast of Africa, where the SAL extends to altitudes of 6 km or higher from the surface.

Amongst the various field experiments conducted in the past couple of decades aiming to study the behavior and properties of desert dust in the SAL (e.g., Heintzenberg, 2009; McConnell et al., 2008; Reid et al., 2003; Siebert et al., 2013; Tanré et al., 2003), the Saharan Aerosol Long-Range Transport and Aerosol-Cloud-Interaction Experiment (SALTRACE) was a particularly recent and comprehensive one (Weinzierl et al., 2017). One remarkable result from SALTRACE was obtained when the same air mass in the SAL was sampled before and after transatlantic transport. This Lagrangian experiment revealed the presence of dust particles as large as ∼30 μm in the Caribbean, whereas the Stokes' settling rate for a laminar environment predicted that no particles larger than ∼7 μm should be able to make it there, even after a correction for particle asphericity (which reduces the deposition rate) was taken into account (Weinzierl et al., 2017).

A few reasons could explain the observed discrepancies and failure of Stokes' law. For one thing, dust particles have very irregular shapes (e.g., Muñoz et al., 2007), which reduces their settling speed due to the increased drag force experimented by dust when compared to a sphere of the same volume (Huang et al., 2020; Mallios et al., 2020). Second, dust becomes electrically charged during its emission and possibly transport, and it has been hypothesized that the resulting electric forces could partly counteract gravitational settling (e.g., Nicoll et al., 2010; Toth III et al., 2020; Van Der Does et al., 2018), although results from a model simulating dust charging mechanisms by Mallios et al. (2022) indicated that the acceleration due to those forces is much smaller than gravity (and hence they should not affect settling speeds). Another reason, which is the focus of this paper, is the possibility of vertical turbulent mixing in the SAL, with the associated upward eddy flux increasing the airborne lifetime of dust particles (Gasteiger et al., 2017; Van Der Does et al., 2018). The inaccurate or absent representation of at least some of these processes might explain why large-scale models consistently tend to underestimate the atmospheric coarse dust loading.

In the SAL, turbulent motion may be forced by both shear and buoyancy mechanisms. Substantial wind shear takes place over West Africa, especially due to the presence of the African Easterly Jet (AEJ) (e.g., Bercos-Hickey et al., 2017). Furthermore, differential absorption and scattering of both short- and long-wave radiation by different size particles could trigger convective motion (Gasteiger et al., 2017; Otto et al., 2007). In fact, recent analyses of lidar and dropsonde data by Gutleben and Groß (2021) revealed small Richardson numbers within the SAL, as well as lidar power spectra following the predicted turbulence slope of −5/3, both of which are indicative of well-established turbulence in that layer.

Furthermore, there exists substantial observational evidence that the SAL is a relatively well-mixed layer, which suggests the presence of turbulence. This includes, for example, lidar profiles of particle linear depolarization ratio (Rittmeister et al., 2017), potential temperature measurements from soundings (Carlson, 2016), as well as aerosol concentration and water vapor mixing ratio profiles from in situ aircraft data (Jung et al., 2013; Ryder, 2021), all of which are rather uniform with height. The effect of daytime convective motion in the SAL was illustrated by Gasteiger et al. (2017) by means of a simple mathematical representation of turbulent mixing. Even though their results suggest that in situ SALTRACE data and satellite-borne lidar measurements are inconsistent with the absence of mixing in the SAL (even when particle asphericity is taken into account), measurement uncertainties were comparable to the differences between calculations that included or neglected mixing. Hence, further research is necessary. Note, however, that it is well-established that turbulence in the Saharan boundary layer (over land) is crucial for the emission and vertical distribution of dust before the elevated SAL is formed (Garcia-Carreras et al., 2015).

More generally, the problem of particles settling in a turbulent environment can be extended to other geophysical situations, with minor modifications necessary in some cases. An instance of an analogous problem to dust in the SAL is that of particles in the ocean mixed layer (OML), such as phytoplankton, sinking into the pycnocline

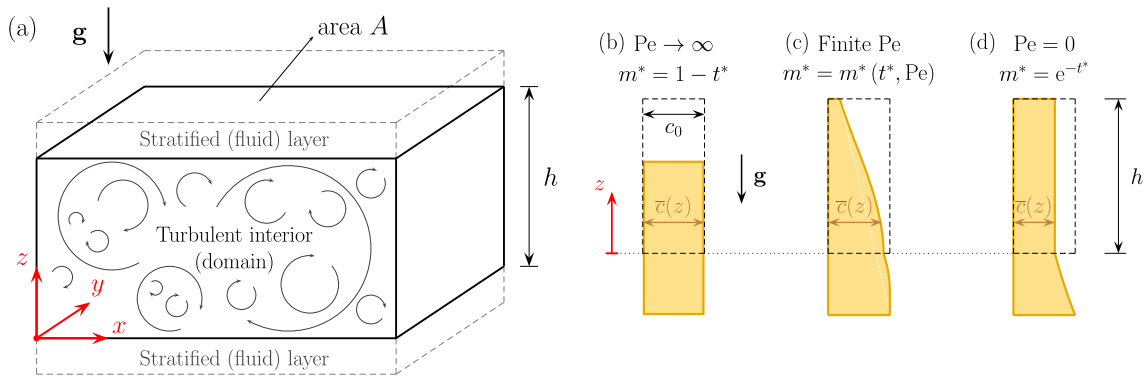


**Figure 1.** (a) Schematic representation of domain geometry. A turbulent, dust-laden fluid layer (region enclosed by black, solid lines, with its base at $z = 0$) of height $h$ is contained in between two stably stratified, laminar fluid layers. (b)–(d) Illustration of theoretical dust profiles at $t^* = 0.4$ for different Peclet numbers (defined in Equation 10). The dashed lines delimit the turbulent layer and indicate the initial dust distribution (uniform from $z = 0$ to $h$), whereas the width of the yellow regions is proportional to the concentration at any level. The dotted line indicates the lower boundary of the Saharan Air Layer, and the flux of dust crossing it is proportional to the concentration at that level (see Equation 5), which in turn depends on the degree of turbulent mixing and the particle size via Pe.

(Deleersnijder et al., 2006; Ruiz, 1996). The long-lasting, global dust storms on Mars are another example of a similar problem that is particularly relevant at present due to the challenges that it poses to the robotic exploration of that planet. In this case, though, the bottom of the flow is a solid boundary, and physical parameters (such as gravity and density) can have very different values as compared to terrestrial flows (Rana et al., 2021). Hence, in this text, phrases like "dust in the SAL" will often be used in situations where ideas also apply more generally to particles settling in turbulent flows, and can potentially be extended to other geophysical problems.

In the present study, we employed a one-dimensional mass balance of dust in the SAL using uniform eddy diffusivity and idealized boundary conditions in order to develop a theory quantifying the effect of turbulent vertical mixing on the settling rate of particles. Because large-eddy simulation (LES) allows for a more realistic representation of the turbulent dynamics by employing fairly universal subgrid-scale models, we verify our theory using LES of a turbulent shear layer which is intended to be a proxy for the flow within the SAL.

This paper is organized as follows. Section 2 presents the idealized mass balance that leads to analytical expressions for airborne aerosol concentration, total mass, and residence time as a function of particle size and turbulent mixing efficiency. The numerical simulations performed are described in Section 3, which also includes information about the simulated particle size bins. LES results are then analyzed and used to validate the theory in Section 4, where we also demonstrate how our model helps explain the long-range transport of super coarse dust observed during SALTRACE. Finally, concluding remarks are made in Section 5.

## 2. Theory

In this section, we develop an exact expression for the total particle mass $m$ (in kg of dust) over time $t$ within a turbulent layer of thickness $h$, given an initially vertically homogeneous concentration field. Two competing effects determine the mass decay rate: gravitational settling and vertical turbulent mixing.

### 2.1. Problem Setup

The idealized flow setup depicted in Figure 1a is intended to be a prototype for the SAL. It is assumed that turbulence is restricted to the inner layer, vanishing at $z \leq 0$ and $z \geq h$ due to stable thermal stratification. Note that, in this coordinate system, $z = 0$ is located above the ground (i.e., there is no solid boundary in this flow).

We assume that the flow is a dilute dispersion so that interactions between particles and the back influence of dust on the flow dynamics are negligible. Denoting the particle velocity vector as $\mathbf{u}_p = (u_p, v_p, w_p)$ in Cartesian coordinates, in which the position vector is $\mathbf{x} = (x, y, z)$, with $z$ being the vertical direction (i.e., that aligned with the acceleration due to gravity $\mathbf{g} = (0, 0, -g)$), conservation of mass for monodispersed particles requires that

$$\partial_t c + \mathbf{u}_p \cdot \nabla c = \kappa \nabla^2 c. \tag{1}$$

In Equation 1, $c$ is the Eulerian particle concentration field (expressed as mass per unit volume), and $\kappa$ is the particle mass diffusivity resulting from Brownian motion.

We further assume that particle inertia effects can be neglected (which is verified a posteriori, as described in Section 3.4 and Appendix B). Then, according to the dusty gas approach (Balachandar & Eaton, 2010), the particle velocity vector can be written as

$$\mathbf{u}_p = \mathbf{u} - w_s\hat{\mathbf{k}}, \tag{2}$$

where $\mathbf{u} = (u, v, w)$ is the instantaneous wind velocity vector, $w_s > 0$ is the constant particle settling velocity (relative to the air), and $\hat{\mathbf{k}} = (0, 0, 1)$.

Rewriting Equation 1 in terms of $\mathbf{u}$ using Equation 2, and applying Reynolds averaging (Pope, 2000, Equation (4.41)), we can write the evolution equation for the mean particle concentration as (Shao, 2008, Equation (8.9))

$$\partial_t\overline{c} + \overline{\mathbf{u}}\cdot\nabla\overline{c} - w_s\partial_z\overline{c} = \kappa\nabla^2\overline{c} - \nabla\cdot\overline{\mathbf{u}'c'}, \tag{3}$$

where the overbar denotes Reynolds averages and the prime indicates fluctuating quantities. The terms on the left-hand side of Equation 3 refer, respectively, to the mean-concentration time trend, advection by the mean flow, and gravitational settling, whereas those on the right-hand side correspond respectively to Brownian diffusion and eddy fluxes (i.e., advection by turbulence).

Brownian diffusion is expected to be negligible compared to gravitational settling for particles larger than ~0.001 μm in the SAL (see calculations in Supporting Information S1). Therefore, the corresponding term in Equation 3 can be safely neglected. For the sake of simplicity, we also disregard subsidence effects by assuming $\overline{w} = 0$. Furthermore, by assuming statistical homogeneity in the horizontal directions (meaning that horizontal gradients of mean concentrations and turbulent fluxes vanish, i.e., $\partial_x\overline{c} = \partial_y\overline{c} = \partial_x\overline{u'c'} = \partial_y\overline{v'c'} = 0$), we obtain the following evolution equation for $\overline{c}$:

$$\partial_t\overline{c} - w_s\partial_z\overline{c} = -\partial_z\overline{w'c'}. \tag{4}$$

Equation 4 is frequently used (with the assumption of stationarity) to model the vertical profile of mean dust concentration in the atmospheric boundary layer (Freire et al., 2016; Kind, 1992; Prandtl, 1952).

We initialize the concentration field with a uniform profile $\overline{c}(z, t = 0) = c_0$ within the turbulent layer $0 < z < h$ and zero elsewhere. This is consistent with the observed well-mixed SAL over the eastern Atlantic (Carlson, 2016). Integrating Equation 4 in the vertical direction from $z = 0$ to $h$, neglecting eddy fluxes across the top and bottom boundaries (such as entrainment/detrainment processes, an assumption expected to hold for larger particles and to be tested with the numerical simulations described in Section 3), and considering that there is no dust above the turbulent layer entering the domain through its top, we find that the particle mass removal rate is given by

$$\frac{1}{A}\frac{\mathrm{d}m}{\mathrm{d}t} = -w_s\overline{c}(z = 0, t), \tag{5}$$

where $A$ is the horizontal area of the domain.

Physically, Equation 5 means that the only particle removal mechanism is gravitational settling through the bottom of the turbulent layer. The removal rate depends on the mean concentration at $z = 0$, which is generally not known a priori, since it comes from the solution to Equation 4. However, there are two limiting cases where $\overline{c}(z = 0, t)$ is known; these are presented in Section 2.2. A closure model for the eddy fluxes in Equation 4, which are responsible for vertical turbulent mixing thereby delaying particle removal, is necessary to generalize the asymptotic results to an arbitrary turbulence intensity. This is discussed in Section 2.3.

### 2.2. Asymptotic Limits: Laminar Flow and Instant Mixing

In the first limiting case, we consider a laminar environment, where turbulent motion is absent. In this scenario, the whole particle field falls as if it were a single solid block, given that no process acts to erode the sharp gradient that develops at the top of the dust layer (Figure 1b). In this case, the concentration at the bottom remains

unchanged and equal to the initial condition at all times, that is, $\overline{c}(z=0,t)=c_0$, and Equation 5 can be integrated to give the linear decay

$$m^*=\begin{cases}1-t^*, & t^*\le 1,\\ 0, & t^*>1\end{cases}\qquad\text{(laminar flow).}\tag{6}$$

In Equation 6, the dimensionless variables are $m^*=m/m_0$ (with $m_0=c_0Ah$, i.e., the initial dust mass) and $t^*=t/\tau_g$ (with $\tau_g=h/w_s$, i.e., the time that it takes for a particle to travel a distance $h$ at speed $w_s$). Note that $\tau_g$ is also the time necessary for all the dust mass to be removed in the absence of turbulence, so that $m^*=0$ for $t^*>1$.

On the other hand, if turbulent mixing is instantaneous, the concentration profile at any instant $t$ is completely well-mixed (Figure 1d). Hence, the concentration at any height (including at $z=0$) equals $m(t)/Ah$, in which case Equation 5 produces the exponential decay

$$m^*=\mathrm{e}^{-t^*}\qquad\text{(instant mixing).}\tag{7}$$

In this case, $\tau_g$ is the $e$-folding time for mass decay. As expected, this means that $m^*$ decays slower than in the laminar case since turbulent mixing is continuously diluting the dust mass throughout the entire layer, thereby reducing the concentration at the bottom and hence the mass loss rate as well.

### 2.3. Exact Solution for Arbitrary Peclet Number

For intermediate mixing rates (i.e., not instantaneous), it is necessary to incorporate a measure of turbulence intensity into Equation 4. Parametrizing the vertical eddy flux in terms of a constant eddy diffusivity $K$ (such that $\overline{w'c'}=-K\partial_z\overline{c}$), Equation 4 becomes

$$\partial_t\overline{c}-w_s\partial_z\overline{c}=K\partial_z^2\overline{c}.\tag{8}$$

Although this is often an unrealistically simple parametrization, a constant $K$ allows for the development of an analytical solution to the problem (to be verified with the simulations described in Section 3). In this model, the requirement that the entrainment fluxes vanish at the boundaries, along with a finite $K$-value, translates into homogeneous Neumann boundary conditions:

$$\partial_z\overline{c}=0\,\text{at}\,z=0\,\text{and}\,h.\tag{9}$$

This also prevents the solution to develop a maximum in the interior of the domain.

Brenner (1962) obtained a series solution for a problem equivalent to Equations 8–9 with a uniform initial condition, which can be used in the problem at hand. Defining the Peclet number as the ratio of a diffusive timescale $\tau_t$ (related to turbulent mixing) to a gravitational settling timescale $\tau_g$, that is,

$$\mathrm{Pe}=\frac{w_sh}{K}=\frac{\tau_t}{\tau_g},\quad \tau_g=\frac{h}{w_s},\quad \tau_t=\frac{h^2}{K},\tag{10}$$

we can write the solution $\overline{c}(z,t)$ as

$$\begin{aligned}\frac{\overline{c}(z^*,t^*,\mathrm{Pe})}{c_0}=&\ \frac{\mathrm{Pe}}{2}\exp\left\{\frac{\mathrm{Pe}}{4}[2(1-z^*)-t^*]\right\}\times\\ &\times\sum_{k=1}^{\infty}\frac{\lambda_k\{\lambda_k\cos[2\lambda_k(1-z^*)]+(\mathrm{Pe}/4)\sin[2\lambda_k(1-z^*)]\}}{\left(\lambda_k^2+\mathrm{Pe}^2/16+\mathrm{Pe}/4\right)\left(\lambda_k^2+\mathrm{Pe}^2/16\right)}\exp\left(-\frac{4\lambda_k^2t^*}{\mathrm{Pe}}\right).\end{aligned}\tag{11}$$

Equation 11 can be integrated within the turbulent layer, that is, from $z^*=z/h=0$ to 1, to find the mass decay over time given by

$$m^*(t^*,\mathrm{Pe})=\frac{\mathrm{Pe}}{4}\exp\left[\frac{\mathrm{Pe}}{4}(2-t^*)\right]\sum_{k=1}^{\infty}\frac{\lambda_k\sin(2\lambda_k)\exp\left(-4\lambda_k^2t^*/\mathrm{Pe}\right)}{\left(\lambda_k^2+\mathrm{Pe}^2/16+\mathrm{Pe}/4\right)\left(\lambda_k^2+\mathrm{Pe}^2/16\right)},\tag{12}$$

where the values of $\lambda_k>0$ ($k=1,2,\ldots$) are implicitly given by

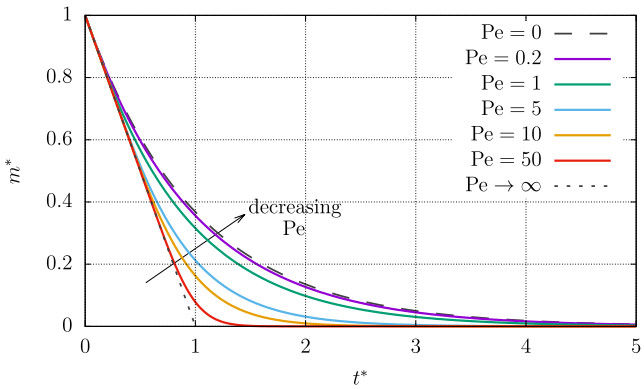


**Figure 2.** Theoretical solutions given by Equation 12 for the remaining particle mass within the turbulent layer over time for different Peclet numbers (colors). The dotted and dashed lines show the asymptotic limits $m^* = 1 - t^*$ and $m^* = \exp(-t^*)$ for $\mathrm{Pe} \to \infty$ and $\mathrm{Pe} = 0$, respectively, as given by Equations 6 and 7.

$$\lambda_{2n-1}\tan(\lambda_{2n-1}) = \frac{\mathrm{Pe}}{4}, \quad \lambda_{2n}\cot(\lambda_{2n}) = -\frac{\mathrm{Pe}}{4} \tag{13}$$

for $n = 1, 2, \ldots$. These values are ordered so that $\lambda_m > \lambda_n$ for $m > n$.

The Peclet number, defined in Equation 10, measures the relative strength of particle gravitational settling with respect to vertical turbulent mixing which, in this model, are the two competing processes determining the airborne lifetime of dust. Hence, the larger (smaller) Pe is, the more (less) gravitational settling dominates over mixing. Note that, when time is normalized by $\tau_g$, the mass decay curve (12), plotted in Figure 2, depends solely on the Peclet number (which accounts for any particular combination of particle size and turbulence intensity). Figure 1c shows an example of an instantaneous concentration profile given by the solution (11) for a finite value of Pe.

As expected, the general solution given in Equation 12 tends to the linear limit of Equation 6 as $\mathrm{Pe} \to \infty$, and it tends to the exponential limit of Equation 7 as $\mathrm{Pe} \to 0$. This fact is also illustrated in the plot of Figure 2, and it can be nicely explained by interpreting Pe as a ratio of timescales. When $\tau_g \ll \tau_t$ ($\mathrm{Pe} \gg 1$), the entire particle field falls as a solid block because individual particles fall much faster than the mixing timescale so the concentration profile is simply advected without changing shape. When $\tau_t \ll \tau_g$ ($\mathrm{Pe} \ll 1$), on the other hand, turbulent mixing is so fast that it is capable of completely mixing the particles within the domain before the particles fall a considerable distance.

As a final remark, it is noteworthy that the series in Equation 12 converges slowly at large Peclet number values. In that case, the alternative, approximate expression for $m^*$ obtained by Brenner (1962) and presented in Appendix A may become useful. Moreover, note that since particles of different sizes are independent of each other in this model, an initial size distribution $m_0(D_p)$, where $D_p$ is the volume-equivalent particle diameter, can easily be evolved in time as $m(t, D_p) = m_0(D_p)m^*(t^*, \mathrm{Pe})$. We highlight that both $t^*$ and Pe depend upon $D_p$ via their dependence on the settling velocity $w_s$ (see Equation 10).

### 2.4. Residence Time

The mean residence time of particles in the turbulent layer can be expressed as (Deleersnijder et al., 2006):

$$\tau_R = \frac{1}{m_0}\int_0^\infty m(t)\,\mathrm{d}t = \tau_g \int_0^\infty m^*(t^*, \mathrm{Pe})\,\mathrm{d}t^*, \tag{14}$$

from where it can be seen that the dimensionless residence time $\tau_R^* = \tau_R/\tau_g$ is a function of the Peclet number only. Integrating the asymptotic solutions given in Equations 6 and 7, one finds that $\tau_R = \tau_g/2$ in the absence of turbulence ($\mathrm{Pe} \to \infty$), whereas $\tau_R = \tau_g$ when mixing is instantaneous ($\mathrm{Pe} = 0$), which means that turbulent mixing can increase the residence time of particles against gravitational settling by a factor of as much as 2 when compared to laminar flow (Deleersnijder et al., 2006).

In order to obtain $\tau_R(\mathrm{Pe})$ for intermediate Pe values, one can integrate Equation 12, which results in

$$\tau_R^*(\mathrm{Pe}) = \frac{1}{16}\mathrm{Pe}^2 \exp\left(\frac{\mathrm{Pe}}{2}\right) \sum_{k=1}^{\infty} \frac{\lambda_k \sin(2\lambda_k)}{\left(\lambda_k^2 + \mathrm{Pe}^2/16 + \mathrm{Pe}/4\right)\left(\lambda_k^2 + \mathrm{Pe}^2/16\right)^2}. \tag{15}$$

However, similarly to Equation 12, the series in Equation 15 converges slowly at large Pe values. Alternatively, a much simpler expression which, unlike the solution above, does not have convergence issues, has been given by Deleersnijder et al. (2006). Namely, they found

$$\tau_R^*(\mathrm{Pe}) = \frac{1}{2} + \frac{1}{\mathrm{Pe}} - \frac{1 - \mathrm{e}^{-\mathrm{Pe}}}{\mathrm{Pe}^2}. \tag{16}$$

As it should, Equation 16 returns the same values as those given by the series in Equation 15. Deleersnijder et al. (2006) obtained that expression by means of an adjoint model approach which does not solve the complete

problem given by Equations 8–9 for $\overline{c}(z,t)$ or $m^*(t)$, but only for $\tau_R$. In other words, their solution does not provide any information on the height dependence or the time evolution of the dust field, which are given in the present study by the series in Equations 11 and 12. Such knowledge is necessary, for instance, in unsteady flows where the eddy diffusivity varies in time, which is likely the case of dust transport in the SAL (considering that it happens over 5 days). In this situation, the residence time can still be estimated via numerical integration of $m^*$ with the Peclet number varying in time, but it will no longer be given by Equation 16.

We highlight that, even at relatively large Peclet numbers, for which the particle behavior is mostly dominated by gravitational settling, the residence time is significantly enhanced by the presence of eddies in the flow. For instance, the relative increase in particle residence time due to turbulent mixing, calculated as $[\tau_R(\mathrm{Pe}) - \tau_R(\infty)]/\tau_R(\infty)$, is 18% for Pe = 10 and 57% for Pe = 2, that is, $\tau_R$ increases respectively by almost a fifth and more than a half of its laminar value in these cases. This suggests that even moderately strong turbulence can considerably impact the settling rate of relatively large particles. As a final remark, notice that Pe is the relevant variable determining the extent to which turbulence impacts dust settling. Translating from Peclet numbers into actual particle sizes, on the other hand, depends on the turbulence intensity of the flow under consideration via $K$ in Equation 10. For approximate SAL conditions, such a relationship is illustrated in Table 2.

## 3. Large-Eddy Simulation of Idealized SAL

### 3.1. Averaging Notation

Before the numerical simulations are described, it is important to define more accurately the notation to be used throughout the rest of the paper. In general, the mean of any variable $\eta$ over a given direction, say $x$, is $\langle\eta\rangle_x$. Reynolds averages $\overline{\eta}$ are considered equivalent to $\langle\eta\rangle_{x,y,t}$, since all simulations are statistically homogeneous in the $x$- and $y$-directions. Averages in $x$ and $y$ are calculated over the entire domain, whereas averaging time periods varied case by case, following the criteria that they must be long enough for statistics to converge, but also short enough so that the turbulence (or the dust field, depending on the statistic being calculated) can still be approximated as stationary. Vertical averages are calculated within the turbulent layer only, that is, $\langle\eta\rangle_z \equiv h^{-1}\int_0^h \eta\,\mathrm{d}z$, and $\langle\eta\rangle_{D_p}$ denotes an average over all simulated particle sizes. Finally, the vertical velocity variance $\overline{w'^2}$ is also denoted as $\sigma_w^2$.

### 3.2. Numerical Specifications of LES Model and Simulation Parameters

Our incompressible LES code employs pseudospectral horizontal derivatives and second-order centered finite-difference derivatives in a staggered grid in the vertical direction. Time is advanced by means of a second-order Adams–Bashforth scheme. The subgrid-scale (SGS) model utilized was the scale-dependent Lagrangian dynamic Smagorinsky model by Bou-Zeid et al. (2005). The dust concentration fields were simulated with the finite-volume approach by Chamecki et al. (2008, 2009), and SGS fluxes of dust were calculated using a constant turbulent Schmidt number Sc = 0.4 (Chamecki et al., 2009, Equations 2–4).

Stress-free boundary conditions were applied to the horizontal velocity components at the top and the bottom of the numerical domain. The vertical velocity $w$ was set to 0 at those positions, and Rayleigh damping was implemented within the stratified layers (above and below the neutral SAL, which is defined by $z \in [0, h]$, as shown in Figure 3) in order to minimize the reflection of gravity waves back into the domain. The thickness of each stratified layer was set to $h/2$, so that they were thick enough to dissipate the wave energy, but still did not needlessly increase the computational cost of the simulations. As a result, the domain vertical extent was $L_z = 2h$. In the horizontal directions, however, the domain is truncated, given the prohibitive computational cost of simulating a flow extending from Africa to the Americas at large-eddy scale resolution. Hence, in the horizontal, we set $L_x = L_y = 4h$.

We used $N^3 = 320^3$ grid points and $h = 1$ km, so that $\Delta x/2 = \Delta y/2 = \Delta z = 6.25$ m. A timestep of $\Delta t = 0.25$ s was chosen for stability and accuracy. Finally, the Coriolis parameter was set to $f = 5 \times 10^{-5}$ s$^{-1}$, which occurs at a latitude of about $\varphi = 20°$N, roughly coinciding with the location where the SAL is generally found in June and July, when the observed transatlantic dust transport typically peaks (Weinzierl et al., 2017).

### 3.3. LES Flow Setup

Temperature profile measurements reveal that the SAL is a nearly neutral layer bounded by inversions at the top and the bottom (e.g., Carlson & Prospero, 1972; Otto et al., 2007). Such observations motivated the potential

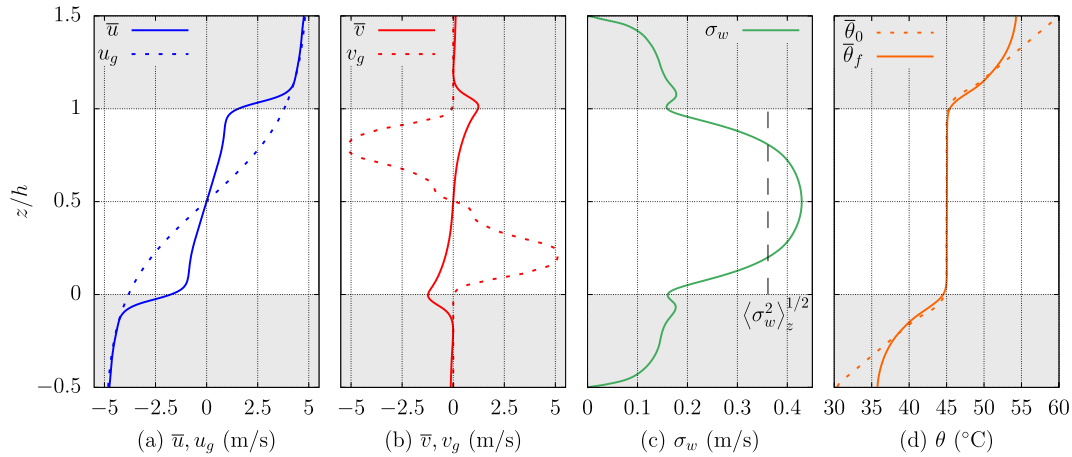


**Figure 3.** Mean large-eddy simulation conditions for BASE flow (WEAK case profiles are presented in Supporting Information S1). The mean horizontal velocity $(\overline{u}, \overline{v})$ and the standard deviation of vertical velocity $\sigma_w$ are calculated using the entire simulation duration (of about 55 hr). The potential temperature profiles shown are ~4-min averages, with $\overline{\theta}_0$ and $\overline{\theta}_f$ denoting respectively the temperature structure at the beginning and the end of the simulation. The mean pressure-gradient force profile driving the flow is prescribed in terms of the geostrophic wind speed $(u_g, v_g)$. The stratified layers, indicated by the gray shaded regions below $z = 0$ and above $z = h$, are not included in the calculation of vertical averages such as $\langle\sigma_w^2\rangle_z^{1/2}$.

temperature structure adopted in our numerical simulations, which is depicted in Figure 3d. The numerical domain includes not only the well-mixed SAL but also part of the inversions above and below it. It does not include, however, the marine boundary layer (MBL) located below the bottom inversion.

Because the inversion layers are statically stable, growth of the turbulent, interior layer by entrainment is effectively suppressed. In fact, it can be seen in Figure 3d that, even though the temperature structure changes significantly over time near the boundaries of the numerical domain due to the imposed adiabatic boundary conditions, stable stratification is preserved close to the inner interfaces between the inversions and the neutral interior. Therefore, the simulated SAL thickness $h$ indeed remained constant in the simulations, and the vertical boundary conditions implemented numerically are of negligible relevance to the turbulence dynamics in the interior. In the horizontal directions, we assume that there is no flux divergence in this truncated domain by adopting periodic boundary conditions in $x$ and $y$.

The mean velocity profiles are plotted in Figures 3a and 3b. Since the Coriolis effect is taken into account, we follow the usual geophysical convention that the $x$-direction points eastward and the $y$-direction points northward. Turbulence was induced in the neutral interior by shear in the mean flow, which in turn was forced by the vertically-varying pressure-gradient force (PGF) prescribed in terms of the geostrophic wind speed $(u_g, v_g)$. Because there is vertical shear in the geostrophic wind, the temperature equation was adapted by means of the change of variables described in Momen et al. (2018) in order to account for the corresponding horizontal temperature gradient arising from thermal wind balance, so that the periodic boundary conditions, implicit to the pseudospectral differentiation scheme, were still valid. Thus, the mean force balance in the interior is similar to that of an Ekman layer, that is, a balance between the PGF, Coriolis force, and Reynolds stresses (not shown). Geostrophic balance is reestablished in the stratified layers where the stratification is strong enough to suppress turbulence.

The mean velocity profile exhibits approximately uniform shear intensity within the neutral interior, causing the turbulence intensity (as given by $\sigma_w$ in Figure 3c) to increase toward the middle of the domain while still being somewhat uniform near the center. The increased shear magnitude at the interior edges of the stratified layers, which occurs as the mean wind transitions to the geostrophic profile, causes a secondary, but much smaller peak in $\sigma_w$ at the same locations. Nevertheless, we did not observe any evidence that this affected the dynamics of dust transport in the interior in any way.

The adopted zonal geostrophic wind profile $u_g(z)$ follows the shape of a hyperbolic tangent, whereas its meridional counterpart $v_g(z)$ was set so as to reduce mean flow rotation and turbulence variability with height. The magnitude of the geostrophic wind, on the other hand, was adjusted so that the resulting mean shear $S$ in the

**Table 1**
*Flow Characteristics in Each Simulation*

| Flow | $\Delta u_g$ (m/s) | $S$ ($s^{-1}$) | $\langle \sigma_w^2 \rangle_z^{1/2}$ (m/s) | $\langle K \rangle_{z,D_p}$ ($m^2/s$) | $\tau_t$ (h) | $\tau_e$ (h) |
|---|---|---|---|---|---|---|
| BASE | 7.62 | $2.91 \times 10^{-3}$ | 0.361 | 32.6 | 8.5 | 0.77 |
| WEAK | 4.57 | $2.27 \times 10^{-3}$ | 0.284 | 25.7 | 10.8 | 0.98 |

*Note.* Here, $\Delta u_g = u_g(z = h) - u_g(z = 0)$, and the amplitude of $v_g(z)$ is proportional to that of $u_g(z)$ in each case. The shear intensity was calculated as $S^2 = \left(d\overline{u}/dz\right)^2 + \left(d\overline{v}/dz\right)^2$ and averaged within the interior, where $S(z)$ is uniform (this excludes the thin, strong-shear layers where the wind transitions to geostrophy). The eddy diffusivity estimation is addressed in Section 4. The mixing timescale $\tau_t$ was calculated from its definition in Equation 10 with $h = 1$ km and $K = \langle K \rangle_{z,D_p}$, whereas the eddy turnover time was estimated as $\tau_e = h\langle \sigma_w^2 \rangle_z^{-1/2}$. Note that $\Delta u_g$ is the only imposed quantity here, as the other variables were diagnosed from the LES output a posteriori.

simulations (see Table 1) was roughly comparable to the typical shear associated with the AEJ, estimated to be about $5 \times 10^{-3}$ $s^{-1}$ (Bercos-Hickey et al., 2020; Cook, 1999; Weinzierl et al., 2017). We note that, if the LES shear is much weaker than the values given in Table 1, the production of turbulence kinetic energy (TKE) is not strong enough to balance its dissipation, and the resulting turbulence is either intermittent or decaying, instead of stationary as desired. Conversely, if the mean shear is much stronger, the turbulent layer grows by entrainment, and $h$ is no longer a constant.

Finally, in an attempt to expand the parameter space analyzed, a similar flow (denoted "WEAK", as opposed to "BASE" previously described) with somewhat weaker turbulence (as its name suggests) was simulated. Results for WEAK are qualitatively similar to those for BASE but with less intense features, since the shape of the geostrophic wind speed profiles was kept the same, but their magnitude was reduced to 60% of their BASE value (see Table 1). The resulting mean flow shear $S$ and vertical velocity standard deviation $\langle \sigma_w^2 \rangle_z^{1/2}$ for WEAK were measured to be about 78.1% and 78.7% of their BASE values, respectively, which suggests the linear scaling $\langle \sigma_w^2 \rangle_z^{1/2} \sim S$. Hence, all figures from 3 to 8 correspond to BASE, but results for WEAK are analogous (WEAK profiles corresponding to Figure 3 are shown in Supporting Information S1). This also served as a check to the similarity solution in Equations 10–13 in terms of the Peclet number, since Pe was also varied by changing the strength of turbulent mixing via $K$, and not only the particle size via $w_s$ (see Tables 1 and 2). The initial thermal structure is the same in both flows. Varying the turbulence intensity even further while keeping the same flow setup can be challenging, given that weaker turbulence dies out, and stronger turbulence causes the inner layer to grow. We also note that the fraction of total momentum (heat) flux represented by the SGS model in BASE is less than 1% (10%) in the SAL interior (except for four levels where the total heat flux changes sign, namely at $z/h \approx 0.1, 0.33, 0.67, 0.9$). Close to the inversion layers at the top and bottom, these fractions approach ~20% for momentum and ~30% for heat.

Both flows were initially simulated for about 3 hr without dust as a spin-up period (which is about four and three large eddy turnover times $\tau_e$ given in Table 1, respectively), which was necessary to achieve equilibrium turbulence from the initial condition $\mathbf{u}_0 = (u_g, 0, 0) + \delta\mathbf{u}_0$, where $\delta\mathbf{u}_0$ is a small-amplitude, random noise. After that,

**Table 2**
*Properties of the Different Size Bins Simulated in Our LES*

| Bin # | 1 | 2 | 3 | 4 | 5 | 6 | 7 | 8 | 9 | 10 | 11 | 12 |
|---|---|---|---|---|---|---|---|---|---|---|---|---|
| $w_s$ (cm/s) | 0.2 | 0.4 | 0.8 | 1.6 | 2 | 2.4 | 3.2 | 4 | 8 | 12 | 16 | 20 |
| $\tau_g$ (h) | 139 | 69.4 | 34.7 | 17.4 | 13.9 | 11.6 | 8.7 | 6.9 | 3.5 | 2.3 | 1.7 | 1.4 |
| $D_p$ ($\mu$m) | 5.8 | 8.2 | 11.6 | 16.5 | 18.4 | 20.2 | 23.4 | 26 | 37 | 46 | 54 | 61 |
| Pe (BASE) | 0.061 | 0.12 | 0.25 | 0.49 | 0.61 | 0.74 | 0.98 | 1.23 | 2.45 | 3.68 | 4.90 | 6.13 |
| Pe (WEAK) | 0.078 | 0.16 | 0.31 | 0.62 | 0.78 | 0.93 | 1.24 | 1.56 | 3.11 | 4.67 | 6.22 | 7.78 |

*Note.* The gravitational timescale $\tau_g$ was calculated from its definition in Equation 10 with $h = 1$ km, and the diameter values $D_p$ were obtained via Equations 17 and18 by assuming aspherical silica dust particles with $\chi = 1.4$ and $\rho_p = 2650$ kg $m^{-3}$ in U.S. standard atmospheric air at about 2 km above the ground where $\rho_f = 1.0$ kg $m^{-3}$, $\mu_f = 1.7 \times 10^{-5}$ Pa s, and $g = 9.8$ m $s^{-2}$. The Peclet number was calculated as $w_s h \langle K \rangle_{z,D_p}^{-1}$ for each flow presented in Table 1.

the dust fields were initialized and simulated for a duration of $T_{LES} \approx 55$ hr for BASE and $T_{LES} \approx 56$ hr for WEAK, corresponding to at least six or five mixing timescales $\tau_t$, respectively. The same particle sizes are simulated in both flows, as described in Section 3.4.

### 3.4. Definition of Dust Size Bins

In addition to the dynamical variables, concentration fields of 12 independent particle size bins (described in Table 2) were also simulated. Each of them was initialized with a uniform profile in the neutral interior and zero elsewhere, that is, the exact same initial condition employed in the one-dimensional mass balance discussed in Section 2. The settling velocities $w_s$ of the simulated bins were chosen to match relevant dust particle sizes and to span a wide range of Peclet numbers.

The various existing numerical simulation techniques for multiphase flows vary in complexity. They include methods that fully resolve the details of the flow around a single particle (Bagchi & Balachandar, 2003; Burton & Eaton, 2005), Lagrangian tracking of point particles using direct numerical simulation data of the carrier fluid (Richter & Chamecki, 2018), and Eulerian approaches, which represent particles in terms of continuous concentration fields. Similarly to the theory described in Section 2, our LES employs the dusty gas approach (Balachandar & Eaton, 2010), which falls into the last category.

The dynamically relevant variable quantifying particle deposition rates, both in the theory and in the LES, is the settling velocity. The functional relationship between $w_s$ and particle size, however, depends on the particle shape. Based on Stokes' law, one can write

$$w_s = \frac{\rho_p g D_{hd}^2}{18 \mu_f \phi(\mathrm{Re}_p)}, \quad \phi(\mathrm{Re}_p) = 1 + 0.15 \mathrm{Re}_p^{0.687}, \quad \mathrm{Re}_p = \frac{\rho_f w_s D_{hd}}{\mu_f}, \tag{17}$$

where $\rho_p$ and $\rho_f$ are, respectively, the particle and the fluid densities, and $\mu_f$ is the fluid dynamic viscosity (Clift et al., 2005, chap. 5). The non-linear correction due to finite particle Reynolds number $\mathrm{Re}_p$ is small but not negligible, and it decreases the estimated $w_s$ by about 10% for the largest particles (those in bin #12, for which $\mathrm{Re}_p = 0.6$).

In Equation 17, we use the effective hydrodynamic diameter $D_{hd}$, defined as the diameter of a spherical particle with the same settling speed as the irregular aerosol of interest (e.g., Westbrook, 2008). Hence, Equation 17 can still be used to determine $w_s$ for aspherical particles such as dust, and their volume-equivalent diameter $D_p$ is related to the effective hydrodynamic diameter via

$$D_p = \chi^{1/2} D_{hd}. \tag{18}$$

In Equation 18, $\chi$ is the dynamic shape factor, that is, the ratio of the actual drag force acting on the irregular aerosol to that experimented by its equivalent-volume sphere (e.g., see Hinds (1999), Equation (3.23) and Huang et al., 2020). Similarly to Weinzierl et al. (2017), we use a value of $\chi = 1.4$ for Saharan dust.

Neglecting particle inertia effects is usually a very good approximation in the atmosphere away from the ground (Richter & Chamecki, 2018), since the Stokes number there is typically very small. After the particle sizes were defined and turbulence measurements from the simulations became available, the applicability of the dusty gas approach adopted in this study (both in the theory and numerical simulations) was confirmed. The Stokes number for our heaviest particles was estimated to be at most $\mathrm{St} \approx 0.07$ in BASE, which has the fastest microscales. Such a value is significantly smaller than the upper limit of $\mathrm{St} = 0.2$ suggested by Balachandar and Eaton (2010) beyond which the dusty gas approach is no longer valid. See Appendix B for more details on the estimation of the relevance of inertial effects in our simulations. Moreover, note that we neglect the slip correction factor in Equation 17 since it is estimated to increase the terminal velocity of the smallest particles simulated in the LES by less than 4%.

## 4. Results and Discussion

### 4.1. Instantaneous Flow Fields

Figures 4 and 5 illustrate the turbulent behavior of the flow with instantaneous snapshots of the dust concentration and fluid vertical velocity fields at $t^* = 1$ for different size particles. The strong fluctuations in vertical velocity

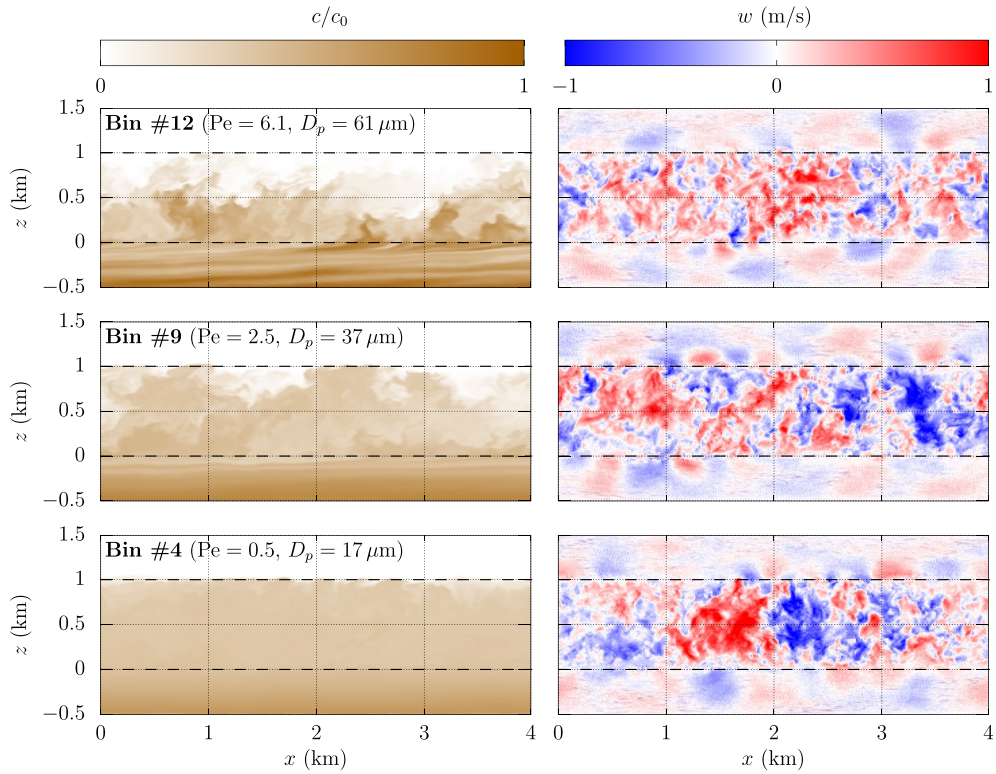


**Figure 4.** Side view of instantaneous dust concentration (left column) and corresponding fluid vertical velocity fields (right column) in BASE at $y = 0.5L_y$ and $t = \tau_g(w_s)$, that is, the instant by which all particles in a given bin would have been removed from the interior ($0 \le z \le 1$ km) if the flow was laminar there. We remark that, in general, the correspondence between Pe and $D_p$ depends upon the turbulent mixing efficiency via $K$.

within the SAL are caused by the turbulent eddies, while those outside the neutral interior are weaker (due to buoyant destruction of TKE) and associated with gravity waves excited by the eddies within the SAL impinging onto the stratified layers. The signature of large eddies in the dust field is clearly visible for bin #12 (for which $w_s$ has comparable magnitude to $\langle\sigma_w\rangle_z$) and still somewhat apparent for bin #9, with regions of positive vertical velocity generally coinciding with regions of high dust concentration. This pattern is not clearly observed for bin #4 though since its Peclet number is much smaller, and hence its concentration remains much more uniform throughout the domain. Note that one also expects the dust field to become uncorrelated with the carrier fluid phase for Pe values much larger than unity (as illustrated in Figure 1b). Moreover, one can also notice in Figure 4 that the largest eddies tend to span the entire turbulent layer (i.e., they scale with $h$), but eddies of many different length scales are present, as is characteristic of turbulent flows in general.

### 4.2. Comparison Between LES and Theory

In order to compare the numerical simulations output data with the theory (i.e., the analytical solutions given by Equations 10–13), one needs to assign a constant eddy diffusivity $K$ to each particle size bin, since this is not defined a priori in the LES, where eddy fluxes are, for the most part, explicitly resolved (with a smaller fraction represented by the SGS model). Thus, two different approaches were utilized to estimate $K$ in this study, as described below.

First, using the time series of aerosol mass within the turbulent layer ($0 < z^* < 1$) obtained by numerical integration of the LES results separately for each size bin, here denoted as $m^*_{LES}(t)$, we looked for the optimal diffusivity $K_\star$ minimizing the mean square error $\mathcal{E}$ with respect to the theoretical solution $m^*$ given by (12), that is,

$$K_\star = \arg\min_K[\mathcal{E}(K)], \quad \mathcal{E}(K) = \frac{1}{T_{LES}}\int_0^{T_{LES}} \left[m^*_{LES}(t) - m^*(t,K)\right]^2 \mathrm{d}t. \tag{19}$$

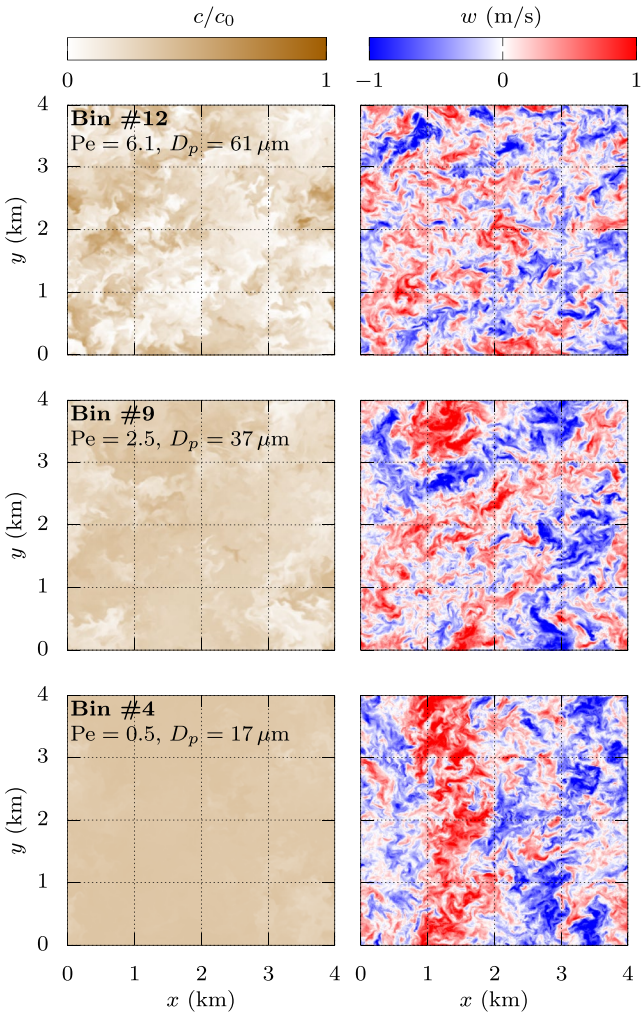


**Figure 5.** Top view of instantaneous dust concentration (left column) and corresponding fluid vertical velocity fields (right column) in BASE at $z = 0.5$ hr and $t = \tau_g(w_s)$ (i.e., same instants shown in Figure 4).

In this sense, $K_\star$ can be regarded as the diffusivity value providing the best fit of the model (12) to the LES data, that is, it determines how close the model can get to the data. Note that $K_\star$ so defined is not only a function of the turbulence but also of the particle size. The theoretical mass decay curves obtained using $\mathrm{Pe} = w_s h K_\star^{-1}$ in Equation 12 are plotted in Figure 6 as gray, solid lines.

Second, we diagnosed profiles of eddy diffusivity $K(z,t)$ from LES data using its definition, that is, $K = -\overline{w'c'}/\partial_z \overline{c}$. Some examples are shown in Figures 7 and 8. Here, $\overline{w'c'}(z)$ and $\overline{c}(z)$ are planar, time averages calculated over a period of duration $T_{avg}$ starting at different instants. The averaging period must be long enough for the statistics to converge, but also relatively small because the dust profiles are very transient, especially for large particles. Hence, we adopted the criterion $T_{avg} \lesssim 0.1\tau_g$, which entails better statistical convergence for smaller particles, for which $\tau_g$ is greater. Despite the substantial time variability of fluxes and gradients, however, a fairly robust diffusivity profile was recovered at all times, so it was natural to take a final time average of those profiles to obtain a single curve $K(z)$ for each bin, some of which are represented by the black squares in Figures 7 and 8.

Since $K$ is assumed to be a constant in our theory, the vertical average of those profiles was also calculated, finally leading to the second eddy diffusivity estimate, denoted simply as $\langle K \rangle_z$. The overall shape of $K(z)$ changes significantly with particle size, with somewhat uniform profiles in the bulk at large Pe values becoming more variable with height as the particle size decreases. However, their mean magnitude $\langle K \rangle_z$, given by the black lines and symbols in Figure 7 through Figure 9, remains relatively robust for all simulated particle sizes. As a result, the diffusivity averaged over all bins $\langle K \rangle_{z,D_p}$ can be taken as representative of the turbulent flow itself. Theoretical mass decay curves obtained using $\mathrm{Pe} = w_s h \langle K \rangle_{z,D_p}^{-1}$ in Equation 12 are plotted in Figure 6 as green, solid lines.

It can be seen in Figure 6 that, with the exception of the small particles (bin #1 and also bin #2, not shown here — see figures for all simulated bins in Supporting Information S1), there is excellent agreement between the LES data and our theory (despite $K$ being assumed constant in the latter). The curves were also plotted in a log scale (on the right column) because the best fit diffusivities $K_\star(D_p)$ provide very similar results to those obtained using $\langle K \rangle_{z,D_p}$, which is a constant, suggesting that the diffusivity dependence on particle size is negligible for this range of Peclet numbers. In fact, $\langle K \rangle_{z,D_p}$ is expected to be a more physical, reliable measure of the diffusivity as opposed to $K_\star$, which depends on the ability of the numerical simulations to reproduce the theoretical solution conditions. This is why Peclet numbers in this paper were calculated using $\langle K \rangle_{z,D_p}$ (unless otherwise stated). Moreover, it can also be seen that the curves progressively approach the exponential limit as the particle size decreases. Therefore, in summary, the LES results validate the analytical model presented in Section 2.

The concentration and flux profiles presented in the two leftmost columns of Figures 7 and 8 are dynamically coupled via Equation 4, which can be re-expressed directly in terms of the variables being plotted as

$$\frac{\partial}{\partial t^*}\left(\frac{\overline{c}}{c_0}\right) = -\frac{\partial}{\partial z^*}\left(\frac{\overline{w'c'}}{w_s c_0} - \frac{\overline{c}}{c_0}\right). \tag{20}$$

It is apparent that, except for very small particles, the analytical solution in Equation 11 for $\overline{c}(z^*, t^*)$ matches the LES data quite well, even though the homogeneous Neumann boundary condition at the top assumed by the model does not seem very applicable to the LES conditions. Concentration estimates obtained from Equation 11 do not match the corresponding LES values near $z = h$, which instead tend to vanish with a non-zero gradient. The simulated eddy fluxes, however, do generally vanish at the boundaries in conformity with the theory.

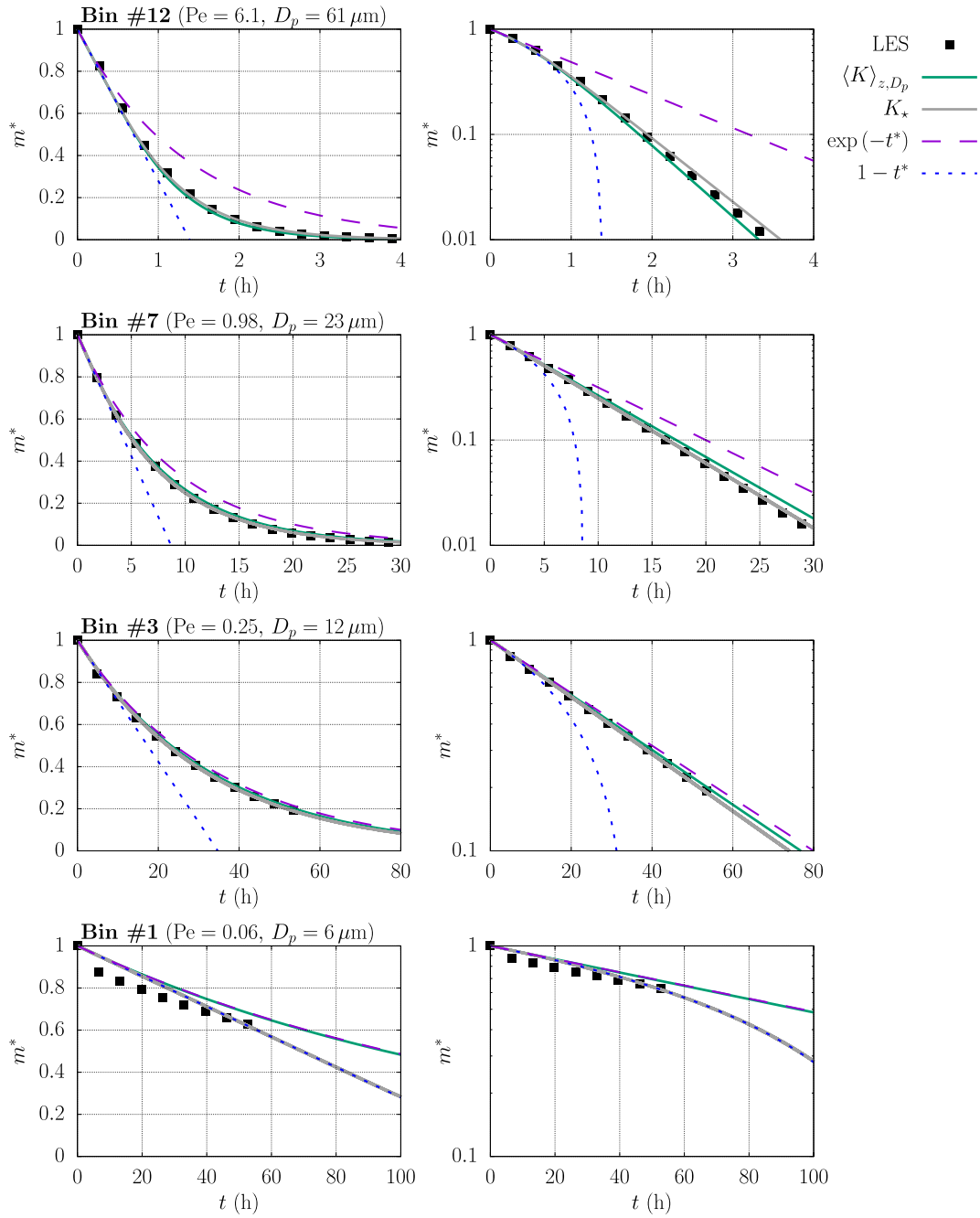


**Figure 6.** Remaining suspended particle mass fraction over time in BASE plotted in linear (left column) and log scales (right column) for different bins. Squares indicate LES values, whereas the solid curves show the theoretical prediction (12) calculated with $K = \langle K \rangle_{z,D_p}$ (average diffusivity diagnosed from large-eddy simulation) and $K = K_\star$ (optimal diffusivity defined in (19)). The linear and exponential asymptotic limits given by Equations 6 and 7 are also plotted for comparison. We remark that, in general, the correspondence between Pe and $D_p$ depends upon the turbulent mixing efficiency via $K$. Plots of $m^*(t)$ for all simulated bins are available in Supporting Information S1.

For small particles, however, a finite eddy flux $\overline{w'c'}$ developed at $z = h$ in the simulations, as is visible in Figure 8 for bins #1 and #2. Those particles "leak" through the shear layer top because they settle very slowly, and the numerical model is not able to maintain a sharp concentration gradient for such a long time. As a result of this additional sink, $m^*_{LES}$ decays faster than our theory allows (see results for bin #1 in Figure 6, and the corresponding concentration profiles in Figure 8). Since this process is not represented by the theory, the analytical solution

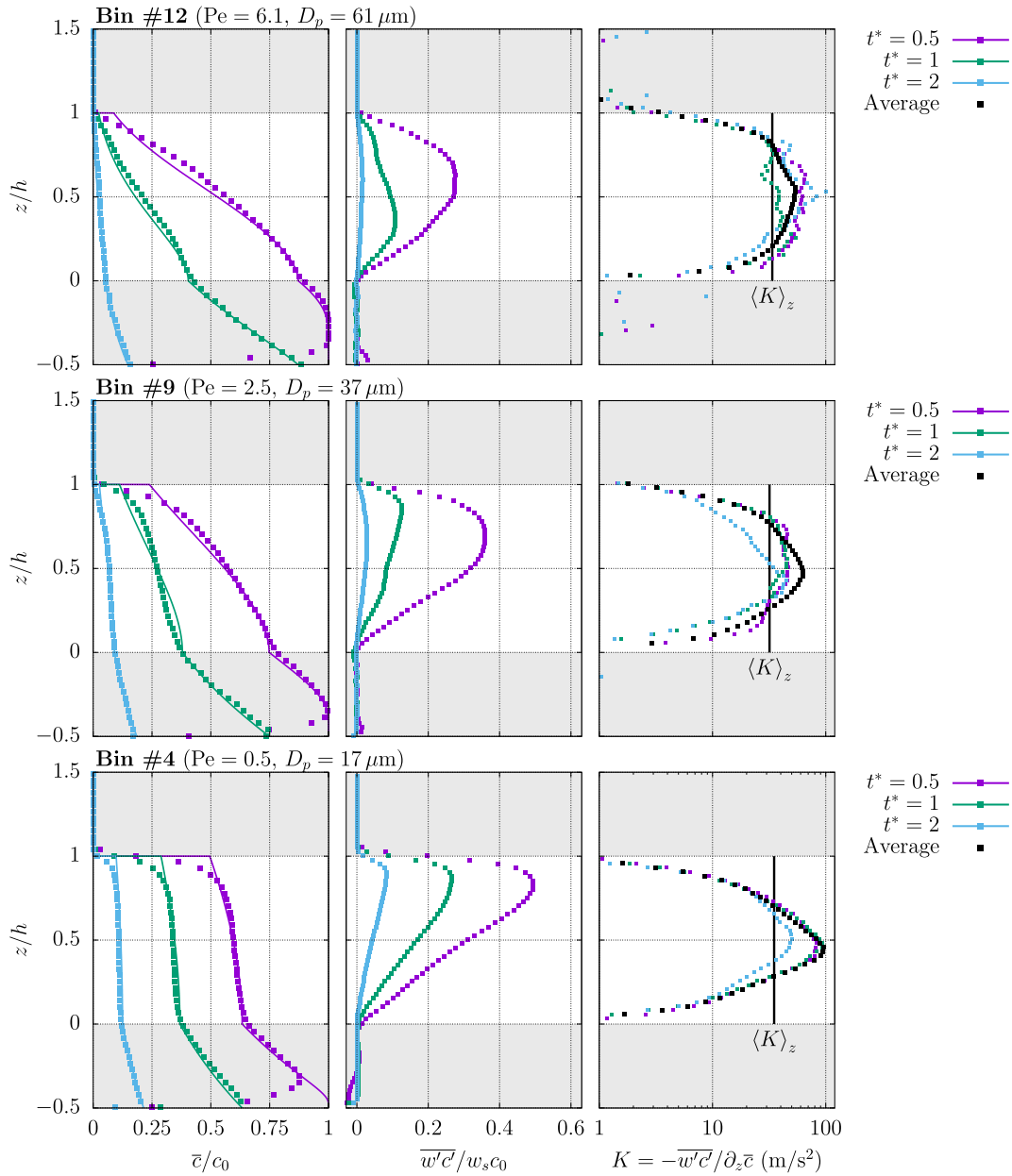


**Figure 7.** Vertical profiles of concentration (left), eddy flux (middle), and eddy diffusivity (right) for different size particles in BASE. Squares indicate large-eddy simulation data, whereas the solid lines on the left panels are the theoretical concentration profiles given by Equation 11 calculated with $K = \langle K \rangle_{z,D_p}$ for $z \in [0, h]$, and advected below the turbulent layer as $\overline{c}(z^* < 0, t^*) = \overline{c}(0, t^* + z^*)$. Although the LES concentrations plotted here are ~4-min averages, the flux and diffusivity profiles are obtained from averages calculated over increasing time intervals $T_{avg}$ for decreasing particle size (but still ensuring that $T_{avg} \lesssim 0.1\tau_g$ for stationarity). The instants $t^*$ shown in the figure correspond to the end of the averaging periods. Vertically-averaged diffusivities $\langle K \rangle_z$ are also shown for each bin. We remark that, in general, the correspondence between Pe and $D_p$ depends upon the turbulent mixing efficiency via $K$.

error $\mathcal{E}$ is thus minimized by a small $K_\star$ value, which instead increases the mass loss rate by reducing the mixing. This is why $m^*$ calculated with $K_\star$ for bin #1 (see Figure 6) coincides with the laminar solution, for which $K = 0$. Furthermore, for small particles, not only is $K(z)$ more variable with height but also the concentration profiles become rather well-mixed, in which case the eddy-diffusivity model is unlikely to perform well since gradients tend to vanish and non-local fluxes due to large eddies become particularly important. All those factors are expected to cause the theory and LES data to mismatch for those bins, leading to unphysical $K_\star$ values which are no longer representative of the diffusivity profiles diagnosed from the LES data. Finally, note that, for even

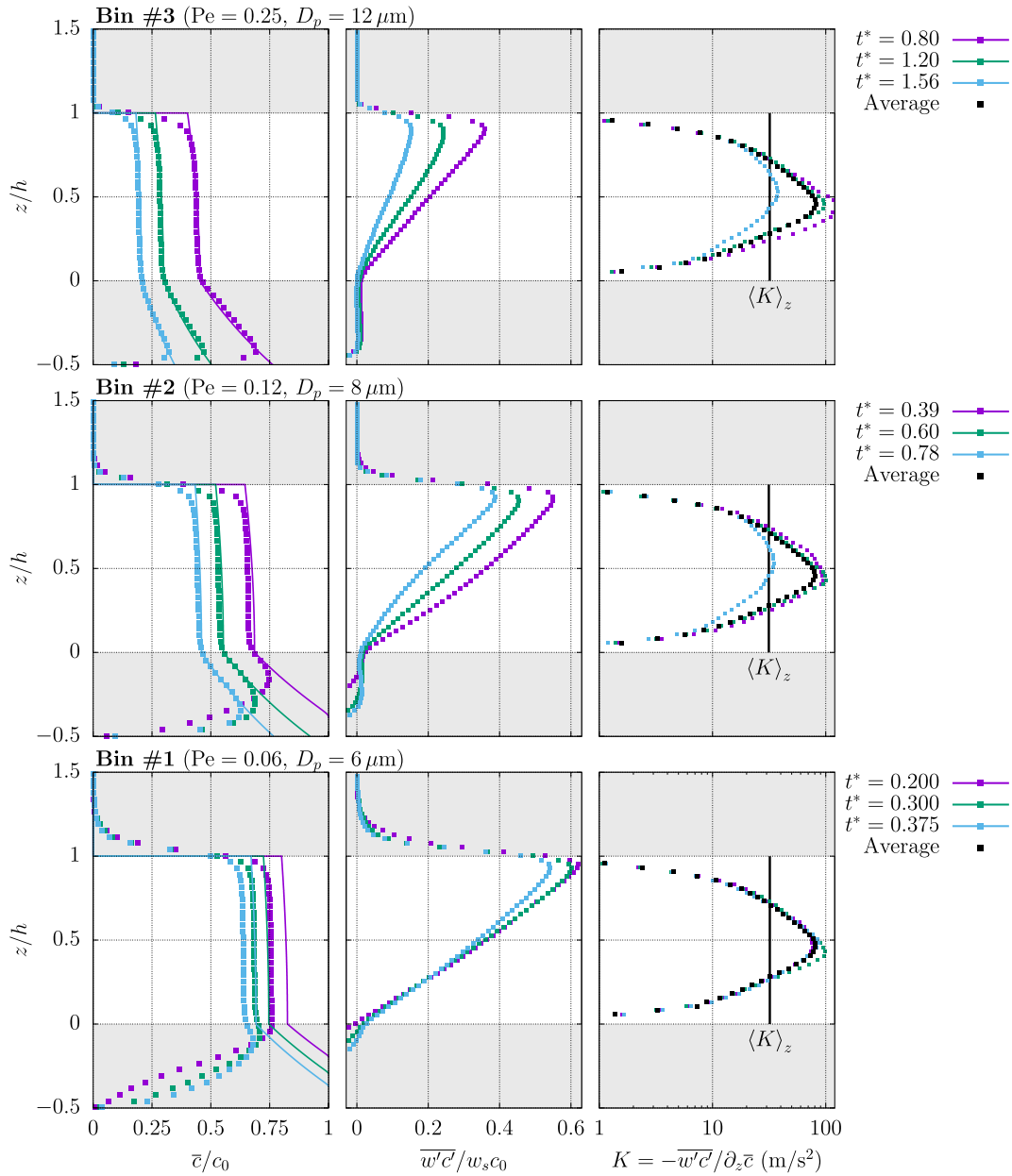


**Figure 8.** Same as Figure 7 but for smaller particles. No-flux condition at $z = h$ is not respected in large-eddy simulation at small Peclet numbers.

smaller particles, removal by detrainment from the turbulent layer may become the dominant mechanism over gravitational settling, which would invalidate the analytical solution for very small Peclet numbers.

### 4.3. *K*-Dependence on Mean Shear and Particle Size

The eddy diffusivity estimates for both simulations were plotted in Figure 9 for different particle sizes as a function of the settling speed normalized by the turbulence intensity as measured by $\left\langle \sigma_w^2 \right\rangle_z^{1/2}$. The average eddy diffusivity $\langle K \rangle_{z,D_p}$ given in Table 1 was verified to scale with $\left\langle \sigma_w^2 \right\rangle_z^{1/2}$, which itself scales linearly with the mean flow shear. Therefore, $K$ was normalized by $h^2 S$ in Figure 9, which to a great extent caused the data to collapse. This is particularly relevant because the intensity of turbulent fluctuations is not a known quantity a priori (based solely

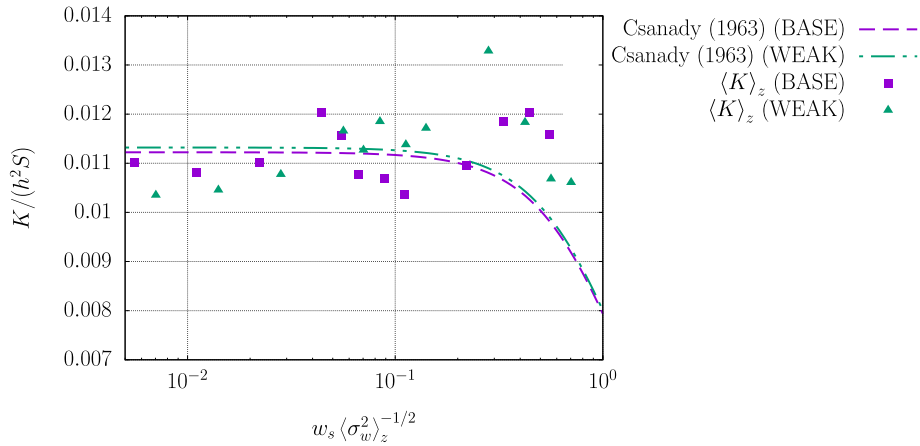


**Figure 9.** Normalized eddy diffusivity as a function of particle size (as given by its normalized settling velocity). The different estimates of $K$ shown are Csanady's model (21) with $K_0 = \langle K \rangle_{z,D_p}$, and the vertically-averaged eddy diffusivity $\langle K \rangle_z$ calculated as $-\left\langle \overline{w'c'}/\partial_z \overline{c} \right\rangle_z$ using LES data. Purple and green curves and symbols correspond respectively to BASE and WEAK data which, despite having different turbulence scales (given in Table 1), collapse after normalization.

on simulation parameters), nor is it readily measurable in the atmosphere with standard meteorological instrumentation. Thus, being able to relate the eddy diffusivity to the mean shear magnitude $S$ has significant practical value. We highlight that both BASE and WEAK simulations are shown in Figure 9 in order to illustrate that normalizing the data by turbulence scales (such as the shear magnitude and the RMS vertical velocity, which are different in each simulation as presented in Table 1) causes the data to collapse. This points to the scaling relation $K \sim S$ as a way to generalize the results obtained in this study for shear flows having different turbulence intensities.

Although we do not have enough data to draw a definite conclusion about such a relationship, the same linear scaling $K \sim S$ is observed in the canonical mixing layer (ML) (Wygnanski & Fiedler, 1970). Hence, it is reasonable to expect that the SAL behaves similarly. Nevertheless, the same shear magnitude produces a smaller eddy flux of momentum $\overline{u'w'}$ in our idealized SAL than it does in a ML, as discussed in Supporting Information S1. This may be attributed to the fact that entrainment of laminar fluid into the shear layer is suppressed in the present study by the temperature inversions, which fundamentally differs from the ML dynamics.

It is expected that heavy particles whose settling speed $w_s$ is comparable to the typical magnitude of turbulent fluctuations $\sigma_w$ decorrelate with the carrier phase velocity due to the crossing-trajectory effect. As a result, their eddy diffusivity decreases, which was modeled by Csanady (1963) as

$$K = K_0 \left( 1 + \beta^2 \frac{w_s^2}{\sigma_w^2} \right)^{-1/2}, \tag{21}$$

where $\beta$ is a constant typically chosen from 1 to 2, and $K_0$ is the diffusivity of non-settling particles. Note that we cannot determine $K_0$ with the flow setup adopted in this study, since $\overline{c} = c_0$ at all times and heights if $w_s = 0$. Instead, we use $K_0 = \langle K \rangle_{z,D_p}$ in order to compare our data with Equation 21. In Figure 9, however, our eddy diffusivity data appears to remain independent of particle size even for $w_s \sim \langle \sigma_w^2 \rangle_z^{1/2}$, instead of following the correction given by Equation 21. This is possibly related to the fact that Equation 21 was derived for homogeneous isotropic turbulence, which is not quite the case for our simulations due to the anisotropic character of the large-scale forcing, as well as the vertical heterogeneity induced by the boundary conditions. Moreover, non-local fluxes are not well represented by an eddy diffusivity closure, and large eddies spanning the entire layer depth $h$ likely contribute significantly to dust transport in the simulated flows.

### 4.4. Implications for Dust Airborne Lifetime and Interpretation of SALTRACE Data

Figure 10a presents the dimensionless residence time $\tau_R^*$ calculated from the analytical solution (16), along with values obtained directly from numerical integration of LES data, as a function of the Peclet number. In the turbulent limit (Pe $\to$ 0), $\tau_R^*$ is twice as large as its laminar limit (Pe $\to \infty$), and most variability occurs in the range 1

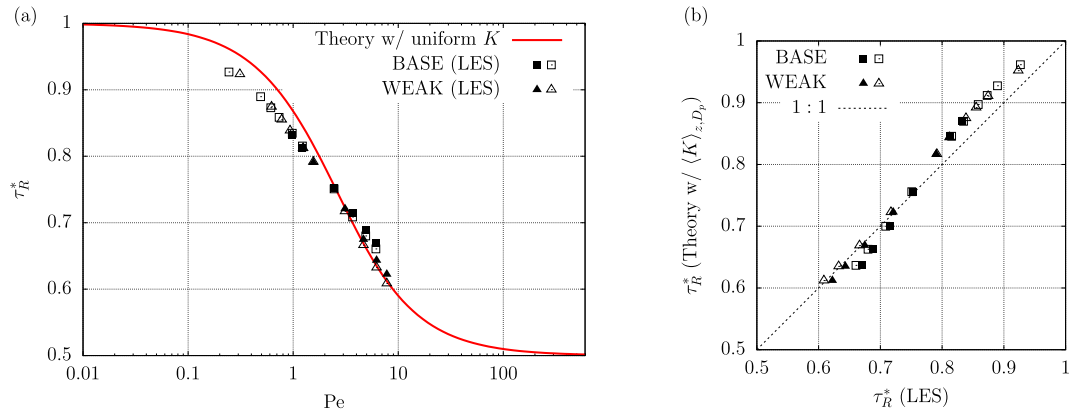


**Figure 10.** (a) Dimensionless residence time as a function of Peclet number as given by exact solution in Equation 16 (red curve) and obtained from numerical integration of $m^*$ curves from large-eddy simulation (LES) for bins #7 through #12 (filled symbols). (b) Theoretical estimate of dimensionless residence time against same quantity obtained via numerical integration of LES data. Squares and triangles correspond respectively to BASE and WEAK. Note that the dimensionless data collapse for both flows, which have different eddy diffusivities, in agreement with the theory (which only depends on Pe). The simulations were not long enough to allow complete removal of particles smaller than those in bin #7, which is why LES estimates were also obtained from integration of the best-fit $m^*$ curves (empty symbols).

$\lesssim$Pe $\lesssim$ 10, which coincides with the range where the Peclet numbers of the converged bins (#7 through #12) are located. The simulations were not long enough for $\tau_R$ to be calculated from its definition in Equation 14 for lighter particles. However, $\tau_R$ was also estimated for bins #3 to #12 by integrating the best-fit $m^*$ curves (labeled "$K_\star$" in Figure 6). These estimates were plotted as hollow symbols in Figure 10. In general, the values obtained from LES data agree well with the theory, as can also be seen in Figure 10b, where both estimates are plotted against each other. Deviations from the theory are slightly larger for smaller Pe (larger residence times), in which case $K$ is a stronger function of $z$ (see Figures 7 and 8), and the assumption of a constant eddy diffusivity may introduce small errors.

Deleersnijder et al. (2006) also derived expressions for $\tau_R^*$(Pe) using non-uniform eddy diffusivity profiles. The resulting residence times, however, were not much different from the values given by Equation 16, which assumes uniform $K$. Instead, their results suggested that $\tau_R$ is rather robust to different diffusivity profiles, depending much more on their magnitude (since $\tau_R^*$ ends up being a function of the Peclet number only). Hence, it is reasonable that, although the diffusivity profiles for the flows simulated in this study decrease toward the laminar layers as shown in Figures 7 and 8, Equation 16 still provided excellent estimates of $\tau_R^*$.

Figure 11a presents the residence time of aerosol particles with volume-equivalent diameter $D_p$ in the LES flows, together with theoretical predictions given by (16) using $K = \langle K \rangle_{z,D_p}$ and $K = 0$, that is, assuming laminar flow, which is intended to represent the estimate of a large-scale model that neglects turbulent mixing. Despite the small deviations of the theory from LES data (which are more visible in Figure 10), it is clear that incorporating the effect of turbulent mixing greatly improves the estimation of the airborne lifetime of aerosols as opposed to assuming laminar flow. This is especially true for small particles, which settle more slowly, and hence are impacted by the eddy motions for longer periods of time. The longer aerosol particles remain airborne, the more likely they are to affect climate and weather via radiative and cloud interactions.

In Figure 11b, the squares indicate the size-resolved, suspended dust concentration ratio between the Caribbean region and West Africa estimated based on SALTRACE measurements. The curves in Figure 11b present model predictions for the same quantity under different assumptions regarding dust asphericity and the presence or absence of turbulent mixing. The observed $c^*$ data plotted here were calculated as the ratio between size distributions obtained in the SALTRACE Lagrangian experiment described in Weinzierl et al. (2017) (more details on the calculations are given in Appendix C). The theoretical estimates were multiplied by a dilution factor $\alpha$ (defined in Equation C5) intended to account for any process not represented in the model described in Section 2 that affects all particle sizes equally. Such processes may include, for instance, horizontal flux divergence (i.e., dilution by lateral entrainment of non-SAL air into the dust plume due to synoptic-scale, horizontal motions in the atmosphere), since an air parcel leaving Africa disperses during

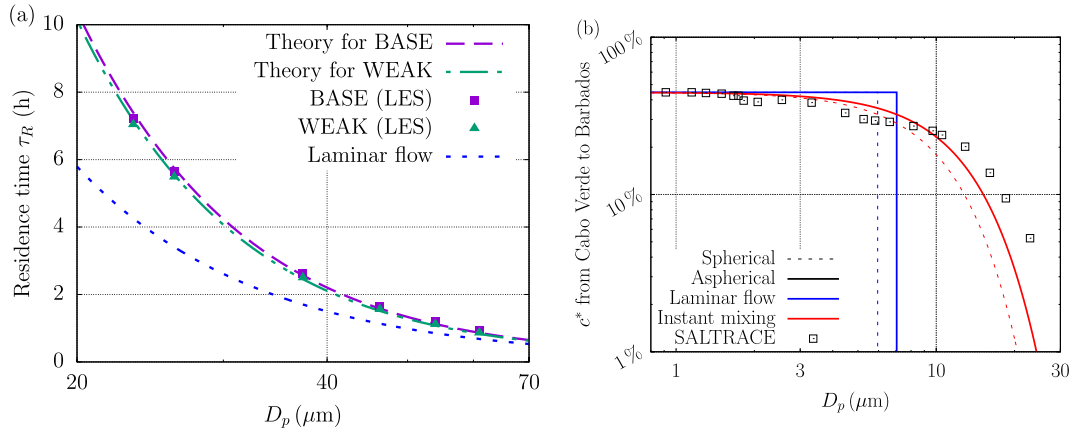


**Figure 11.** (a) Residence time (in hours) as a function of dust geometric diameter $D_p$ obtained from our LES (squares and triangles for BASE and WEAK, respectively, illustrating different turbulence intensities), Equation 16 with $\mathrm{Pe} = w_s h \langle K \rangle^{-1}_{z,D_p}$ (purple and green dashed lines), and the corresponding estimate when turbulent mixing is neglected (dotted blue line). (b) Size-resolved mass concentration ratio of dust particles remaining airborne from Cabo Verde to Barbados (squares) calculated based on Saharan Aerosol Long-Range Transport and Aerosol-Cloud-Interaction Experiment data (Weinzierl et al., 2017; Figure 9) and model predictions assuming the presence and absence of turbulence, spherical and aspherical particles with $\chi = 1.4$, and a SAL thickness of $h = 4$ km. The calculations refer to particles reaching a measurement level located 1.3 km below the SAL top in Barbados. Theoretical estimates for $c^*$ are multiplied by a constant factor $\alpha$ (see Equations C5–C8) so as to match the measured data at small $D_p$, which is intended to account for plume dilution and any size-independent processes acting to reduce the concentrations measured in Barbados.

its transatlantic transport and reaches several different locations in the Americas, as well as entrainment into the boundary layer and wet deposition. Downward turbulent mixing of dust at the SAL base into the MBL is known to be an effective dust removal mechanism from the SAL (Carlson & Prospero, 1972; Rittmeister et al., 2017; Weinzierl et al., 2017), and LES of the boundary layer performed by Jähn et al. (2016) confirmed that it takes place in the Caribbean region at a rate dependent upon the magnitudes of the wind shear and temperature inversion between the SAL and the MBL. In fact, wet deposition and convective (turbulent) removal dominate in the Caribbean, whereas dry deposition is more important closer to the North African source regions (Ridley et al., 2012).

Despite the actual complexity of reality, which must be accurately represented if one is to explain measurements in detail, Figure 11b shows that this simple model, which accounts for particle shape and turbulent mixing, explains to a good extent the otherwise rather surprising presence of super coarse Saharan dust in Barbados. Hence, incorporating the effects of free atmospheric turbulence and particle asphericity in large-scale models presents significant potential for improvement in aerosol long-range transport modeling. Note that, in the laminar case, accounting for particle asphericity simply shifts the largest particle size by a factor of $\chi^{1/2}$ (the well-mixed case is discussed in detail in Supporting Information S1).

Several reasons might help explain the remaining discrepancy between models and measurements of coarse dust in Figure 11b. For instance, size-dependent processes other than dry deposition, such as cloud processing, which contributes to producing larger particles (Wurzler et al., 2000), are capable of altering the dust size distribution in the SAL. Hence, it is possible that the dilution effect was overestimated, and multiplying the model estimates by a factor closer to unity instead would indeed make the theoretical curves approach the observations. Other possible factors leading to a mismatch between the model and observations include horizontal variability of dust concentration measured in the SAL, the detection of additional aerosol from different sources in the Caribbean, and the effect of electric forces counteracting gravity, not to mention other sources of uncertainty intrinsic to field measurements.

We highlight that simple knowledge of the residence time given by Equation 16 is not enough to determine the suspended aerosol concentration fraction $c^* = \alpha m^*$ at a given instant $t$ and height $z$ as plotted in Figure 11b, which underlines the relevance of the complete analytical solution for $c^*$ given by Equation 11. Moreover, Equation 12 can be used to compute the difference $\Delta m^*$ between the actual airborne dust mass fraction at any given time and $m^*$ in a laminar flow at the same instant, that is,

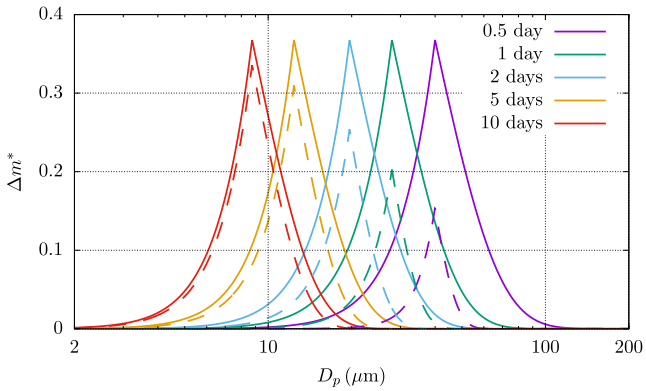


**Figure 12.** Additional Saharan Air Layer dust mass fraction as a result of turbulent mixing according to Equation 12 in a layer of thickness $h = 4$ km after different travel times (colors) for instant mixing, that is, $K \to \infty$ (solid lines), and $K = 32.6$ m$^2$/s (dashed lines).

$$\Delta m^* = \begin{cases} m^*(t^*, \mathrm{Pe}) - (1 - t^*), & t^* \le 1, \\ m^*(t^*, \mathrm{Pe}), & t^* > 1. \end{cases} \tag{22}$$

This is illustrated for different travel times $t$, eddy diffusivities $K$, and particle sizes $D_p$ in Figure 12. First, note that, while the effect of turbulence on the dust airborne lifetime increases monotonically with decreasing particle size (see Equation 16, and Figures 10a and 11a), $\Delta m^*$ has a maximum at intermediate particle sizes. After a given transport time, small enough particles are not affected by turbulence because they barely settle. Since in this case, no gradient develops for turbulent mixing to act on, $\Delta m^*$ tends to zero as the particle size decreases. For example, note in Figure 11b that the curves for laminar and turbulent flow coincide for $D_p \lesssim 3$ μm. On the other hand, $\Delta m^*$ also vanishes for large enough particles at long enough times, in which case all particles of a given size are completely removed from the SAL, no matter how strong the turbulent mixing is. For instance, one can see in Figure 11b that particles greater than about 30 μm are completely removed after the 5-day window in both laminar and instant-mixing conditions. As a result, $\Delta m^*$ peaks at intermediate particle sizes. In the case of the SALTRACE Lagrangian experiment, we notice that the 5-day curve in Figure 12 indeed shows that $\Delta m^*$ peaks for $D_p$ in the range 10–20 μm.

The peak in $\Delta m^*$ occurs at $t^* = 1$, regardless of the value of $K$. This means that, at any time $t$, particles with $w_s = h/t$ are the most affected by turbulent mixing. In other words, the instant when the effect of turbulence on a given particle size can be most appreciated is $t = \tau_g$, that is, when gravity would have finished removing those particles from a laminar SAL. Therefore, at shorter times, heavier particles are more affected, whereas smaller particles are more affected over longer times. Finally, while $\Delta m^*(D_p)$ is greatest when $K \to \infty$ (always peaking at $\Delta m^* = e^{-1}$ at $t^* = 1$), it is smaller for finite diffusivity values. In this case, $\Delta m^*$ increases with increasing travel times (as turbulent mixing has more time to act), therefore impacting small-Pe particles more significantly.

## 5. Conclusions

In spite of the importance of coarse desert dust in the Earth system, current models consistently underestimate its concentration in the atmosphere. With this motivation, the present study employed a simple advection-diffusion model to represent the competing effects of settling and turbulent mixing on the suspended lifetime of dust in the SAL. The results were validated with LES data for particles in a turbulent shear layer contained between stable inversions (much like the SAL). Despite the height dependence of the eddy diffusivity and the potential contribution of non-local fluxes (both factors being especially relevant for small particles) in the numerical simulations, this simple model provided reasonable estimates for low-order moments and integral measures such as the size-resolved suspended aerosol mass over time, as well as the concentration profiles and residence time of particles in the atmosphere. However, this model may become inadequate for very small particles whose dominant removal mechanism from the turbulent layer is detrainment (rather than gravitational settling).

The particle airborne lifetime $\tau_R$ depends solely on the particle Peclet number, is rather independent of the diffusivity profile, and can increase by up to a factor of 2 due to turbulent mixing when compared to laminar flow. A constant diffusivity value, scaling with the flow mean shear, that is, $K \sim S$, was enough to describe the behavior of all size bins, though it is possible that this is no longer the case for particles larger than those considered in this study, for which the crossing-trajectory effect may start manifesting.

Furthermore, our simplified analytical representations of turbulent mixing and aerosol asphericity were able to explain to a considerable extent the presence of super coarse Saharan dust in the Caribbean observed in the SALTRACE Lagrangian experiment measurements. Nevertheless, this coarse dust long range transport conundrum is not yet completely solved, and the problem requires further investigation. A better particle shape parametrization, as well as a model including electric forces, may bring theoretical estimates closer to observations.

Moving forward, it might be of interest to add other processes to the prototype turbulent shear flow simulated in the present study, so that it becomes a more realistic representation of some particular flow of interest. For instance,

one can incorporate buoyancy effects (including feedback from the dust field due to particle-radiation interaction) to simulate the SAL more accurately. In fact, a more complete SAL representation needs also to include realistic PGF profiles, which could be utilized in order to determine whether turbulence actually develops in the SAL and what the associated TKE budget is. In the Caribbean region, however, deep convection, wet deposition, and mixing with the boundary layer also play a fundamental role in the fate of the dust size distribution, and the flow dynamics is expected to be rather different from that of the numerical simulations presented in this study.

## Appendix A: Asymptotic Solution for Large Peclet Numbers

At large Pe values, the series solution Equation 12 converges slowly. A useful alternative expression (Brenner, 1962) for mass decay is then given by

$$m^*(t^*, \mathrm{Pe}) \sim M_1(t^*, \mathrm{Pe}) + M_2(t^*, \mathrm{Pe}) - M_3(t^*, \mathrm{Pe}) \quad \text{as} \quad \mathrm{Pe} \to \infty, \tag{A1}$$

where

$$M_1 = (1 - t^*)\left\{1 - \frac{1}{2}\mathrm{erfc}\left[\sqrt{\frac{\mathrm{Pe}}{4t^*}}(1 - t^*)\right]\right\} + \frac{\mathrm{e}^{\mathrm{Pe}}}{2}(1 + t^*)\mathrm{erfc}\left[\sqrt{\frac{\mathrm{Pe}}{4t^*}}(1 + t^*)\right], \tag{A2}$$

$$M_2 = \frac{1}{3}\sqrt{\frac{\mathrm{Pe}t^*}{\pi}}\left[2t^* + 3(1 + t^*) + \frac{\mathrm{Pe}}{2}(1 + t^*)^2\right]\times \times\left\{\exp\left[-\frac{\mathrm{Pe}(1 - t^*)^2}{4t^*}\right] - \exp\left[-\frac{\mathrm{Pe}\left(4 + t^{*2}\right)}{4t^*}\right]\right\}, \tag{A3}$$

$$M_3 = \mathrm{e}^{\mathrm{Pe}}\left[t^* + \frac{\mathrm{Pe}}{2}t^*(1 + t^*) + \frac{\mathrm{Pe}}{2}(1 + t^*)^2 + \frac{\mathrm{Pe}^2}{12}(1 + t^*)^3\right]\times \times\left\{\mathrm{erfc}\left[\sqrt{\frac{\mathrm{Pe}}{4t^*}}(1 + t^*)\right] - \mathrm{erfc}\left[\sqrt{\frac{\mathrm{Pe}}{4t^*}}(2 + t^*)\right]\right\}. \tag{A4}$$

## Appendix B: Significance of Particle Inertia

From Table 2, our largest particle has response time $\tau_p = w_s/g = 0.0204$ s and diameter $D_p = 61.0$ μm. In BASE, where turbulence is stronger, the TKE dissipation rate measured from the LES output peaks near the domain center at a value of $\varepsilon = 1.96 \times 10^{-4}$ m$^2$ s$^{-3}$. The corresponding Kolmogorov length and time scales in the atmosphere (assuming air with kinematic viscosity $\nu = \mu_f/\rho_f = 1.7 \times 10^{-5}$ m$^2$ s$^{-1}$) are hence $\eta_K = \left(\nu^3/\varepsilon\right)^{1/4} = 2.24$ mm and $\tau_K = \sqrt{\nu/\varepsilon} = 0.295$ s. Therefore, our greatest Stokes number is $\mathrm{St} = \tau_p/\tau_K = 0.069$, which is significantly smaller than the value of St = 0.2 suggested by Balachandar and Eaton (2010) as the maximum Stokes number for which the dusty gas approach is still a reasonable approximation.

Furthermore, assuming that the LES filter scale, given by $\Delta = (\Delta x \Delta y \Delta z)^{1/3} = 9.92$ m, occurs in the inertial subrange where Kolmogorov scaling is valid, the timescale of the smallest resolved eddy in BASE is estimated as $\tau_\Delta = \tau_K(\Delta/\eta_K)^{2/3} = 79.5$ s. Hence, $\tau_p/\tau_\Delta \lesssim 3 \times 10^{-4}$ in our simulations, which is less than the maximum acceptable value of $10^{-3}$ for that ratio provided by Balachandar and Eaton (2010) (Figure 2) for LES using the dusty gas approach. Moreover, $D_p/\eta_K \lesssim 3 \times 10^{-2}$ in our simulations, that is, all simulated particles are much smaller than the Kolmogorov lengthscale (and thus also much smaller than the smallest resolved eddies in the LES), so the point-particle approximation, implicit in the dusty gas approach, is also valid.

In conclusion, particle inertia effects can be safely neglected in this study, since the response time of the heaviest simulated particles is still much smaller than the timescale of the fastest, smallest resolved eddies. Therefore, (3) is a good model for the problem at hand.

## Appendix C: Calculation of $c^*(D_p)$ with SALTRACE Data and Theory

If we denote the airborne dust mass in the Cabo Verde and Barbados regions as $m_0$ and $m_f$ respectively, we can write

$$m^* = \frac{m_f}{m_0} = \frac{c_f\,\delta V_f}{c_0\,\delta V_0}, \tag{C1}$$

where $c$ and $\delta V$ respectively refer to the mass concentration and the volume of a Lagrangian fluid element at each location. Defining a plume spread coefficient as $\alpha_v = \delta V_0/\delta V_f$ (where $\alpha_v < 1$ due to entrainment of non-SAL air into the plume), we can relate the mass ratio to the concentration ratio $c^* = c_f/c_0$ at the two locations via

$$c^* = \alpha_v m^*. \tag{C2}$$

In order to relate mass concentration $c$ to number concentration $n$, we write

$$c(D_p) = n(D_p) \times \underbrace{\rho_p(D_p)}_{\text{particle density}} \times \underbrace{\left(\frac{1}{6}\pi D_p^3\right)}_{\text{particle volume}}, \tag{C3}$$

where, by definition, the volume-equivalent diameter $D_p$ is used to calculate the volume for any particle shape. With the assumption that $\rho_p(D_p)$ remains unchanged from Cabo Verde to Barbados, we have that

$$c^*(D_p) = \frac{n_f(D_p)}{n_0(D_p)}. \tag{C4}$$

The number size distributions $n_0$ and $n_f$ were obtained from SALTRACE measurements (Weinzierl et al., 2017; Figure 9) in order to generate Figure 11b.

We further assume that dry deposition is negligible for the smallest particle size available in the data. This is confirmed by Figure 12, which shows that particles with $D_p < 2$ μm have negligible settling after around 5 days of transport. However, we also need to consider the possibility that, even for those small particles, $m^* = \alpha_0 < 1$ due to processes other than entrainment of non-SAL air into the plume (e.g., wet deposition). Under the assumption that these processes affect all particle sizes equally, we accounted for their effect by calculating the concentration fraction as $c^* = \alpha m^*$, where $\alpha$ is an overall dilution factor estimated as

$$\alpha = \alpha_0\alpha_v = \left.\frac{n_f}{n_0}\right|_{\text{smallest } D_p} \approx 0.447. \tag{C5}$$

If concentration measurements are taken at a height $z_m$ from the SAL base at an instant $t_m$, assuming a well-mixed initial profile, theory for the laminar case predicts that

$$c^*(D_p) = \begin{cases} \alpha, & D_p \le D_{p,\max}, \\ 0, & D_p > D_{p,\max}, \end{cases} \tag{C6}$$

where the maximum diameter is given implicitly by

$$w_s(D_{p,\max}) = \frac{h - z_m}{t_m}. \tag{C7}$$

As described in Weinzierl et al. (2017), for a travel time of $t_m = 5$ days, the greatest particle size to be detected at a distance $h - z_m = 1.3$ km from the SAL top is that with settling velocity $w_s = 0.26$ km day$^{-1}$ which, according to Equations 17 and 18 and the values given in table 2, corresponds to $D_{p,\max} = 7.05$ μm. The well-mixed limit, on the other hand, predicts that

$$c^*(D_p) = \alpha \exp\left[-\frac{w_s(D_p)t_m}{h}\right]. \tag{C8}$$

Equations C6–C8 were used to plot the theoretical curves in Figure 11b.

## Data Availability Statement

The data required to reproduce the figures are available from the Dryad repository at the assigned https://doi.org/10.5068/D11D5D.

**Acknowledgments**
We would like to acknowledge high-performance computing support from Cheyenne (https://doi.org/10.5065/D6RX99HX) provided by NCAR's Computational and Information Systems Laboratory, sponsored by the National Science Foundation. This material is based upon work supported by the National Science Foundation under Grant 1856389.

## References

Adebiyi, A. A., & Kok, J. F. (2020). Climate models miss most of the coarse dust in the atmosphere. *Science Advances*, *6*(15), eaaz9507. https://doi.org/10.1126/sciadv.aaz9507

Bagchi, P., & Balachandar, S. (2003). Effect of turbulence on the drag and lift of a particle. *Physics of Fluids*, *15*(11), 3496–3513. https://doi.org/10.1063/1.1616031

Balachandar, S., & Eaton, J. K. (2010). Turbulent dispersed multiphase flow. *Annual Review of Fluid Mechanics*, *42*(1), 111–133. https://doi.org/10.1146/annurev.fluid.010908.165243

Bercos-Hickey, E., Nathan, T. R., & Chen, S.-H. (2017). Saharan dust and the african easterly jet–african easterly wave system: Structure, location and energetics. *Quarterly Journal of the Royal Meteorological Society*, *143*(708), 2797–2808. https://doi.org/10.1002/qj.3128

Bercos-Hickey, E., Nathan, T. R., & Chen, S.-H. (2020). On the relationship between the african easterly jet, saharan mineral dust aerosols, and west african precipitation. *Journal of Climate*, *33*(9), 3533–3546. https://doi.org/10.1175/jcli-d-18-0661.1

Bou-Zeid, E., Meneveau, C., & Parlange, M. (2005). A scale-dependent Lagrangian dynamic model for large eddy simulation of complex turbulent flows. *Physics of Fluids*, *17*(2), 025105. https://doi.org/10.1063/1.1839152

Brenner, H. (1962). The diffusion model of longitudinal mixing in beds of finite length. numerical values. *Chemical Engineering Science*, *17*(4), 229–243. https://doi.org/10.1016/0009-2509(62)85002-7

Burton, T. M., & Eaton, J. K. (2005). Fully resolved simulations of particle-turbulence interaction. *Journal of Fluid Mechanics*, *545*(-1), 67–111. https://doi.org/10.1017/s0022112005006889

Carlson, T. N. (2016). The saharan elevated mixed layer and its aerosol optical depth. *The Open Atmospheric Science Journal*, *10*(1), 26–38. https://doi.org/10.2174/1874282301610010026

Carlson, T. N., & Prospero, J. M. (1972). The large-scale movement of saharan air outbreaks over the northern equatorial atlantic. *Journal of Applied Meteorology and Climatology*, *11*(2), 283–297. https://doi.org/10.1175/1520-0450(1972)011<0283:tlsmos>2.0.co;2

Chamecki, M., Meneveau, C., & Parlange, M. B. (2008). A hybrid spectral/finite-volume algorithm for large-eddy simulation of scalars in the atmospheric boundary layer. *Boundary-Layer Meteorology*, *128*(3), 473–484. https://doi.org/10.1007/s10546-008-9302-1

Chamecki, M., Meneveau, C., & Parlange, M. B. (2009). Large eddy simulation of pollen transport in the atmospheric boundary layer. *Journal of Aerosol Science*, *40*(3), 241–255. https://doi.org/10.1016/j.jaerosci.2008.11.004

Chien, C.-T., Mackey, K. R., Dutkiewicz, S., Mahowald, N. M., Prospero, J. M., & Paytan, A. (2016). Effects of african dust deposition on phytoplankton in the Western tropical atlantic ocean off Barbados. *Global Biogeochemical Cycles*, *30*(5), 716–734. https://doi.org/10.1002/2015gb005334

Clift, R., Grace, J. R., & Weber, M. E. (2005). Bubbles, drops, and particles.

Computational & Information System Laboratory. (2019). *Cheyenne: HPE/SGI ICE XA system (climate simulation Laboratory)*. National Center for Atmospheric Research. https://doi.org/10.5065/D6RX99HX

Cook, K. H. (1999). Generation of the African easterly jet and its role in determining West African precipitation. *Journal of Climate*, *12*(5), 1165–1184. https://doi.org/10.1175/1520-0442(1999)012<1165:gotaej>2.0.co;2

Csanady, G. (1963). Turbulent diffusion of heavy particles in the atmosphere. *Journal of the Atmospheric Sciences*, *20*(3), 201–208. https://doi.org/10.1175/1520-0469(1963)020<0201:tdohpi>2.0.co;2

Deleersnijder, E., Beckers, J.-M., & Delhez, E. J. (2006). The residence time of settling particles in the surface mixed layer. *Environmental Fluid Mechanics*, *6*(1), 25–42. https://doi.org/10.1007/s10652-005-3941-2

DeMott, P. J., Sassen, K., Poellot, M. R., Baumgardner, D., Rogers, D. C., Brooks, S. D., et al. (2003). African dust aerosols as atmospheric ice nuclei. *Geophysical Research Letters*, *30*(14). https://doi.org/10.1029/2003gl017410

Freire, L., Chamecki, M., & Gillies, J. (2016). Flux-profile relationship for dust concentration in the stratified atmospheric surface layer. *Boundary-Layer Meteorology*, *160*(2), 249–267. https://doi.org/10.1007/s10546-016-0140-2

Garcia-Carreras, L., Parker, D., Marsham, J., Rosenberg, P., Brooks, I., Lock, A., et al. (2015). The turbulent structure and diurnal growth of the saharan atmospheric boundary layer. *Journal of the Atmospheric Sciences*, *72*(2), 693–713. https://doi.org/10.1175/jas-d-13-0384.1

Gasteiger, J., Groß, S., Sauer, D., Haarig, M., Ansmann, A., & Weinzierl, B. (2017). Particle settling and vertical mixing in the saharan air layer as seen from an integrated model, lidar, and in situ perspective. *Atmospheric Chemistry and Physics*, *17*(1), 297–311. https://doi.org/10.5194/acp-17-297-2017

Gutleben, M., & Groß, S. (2021). Turbulence analysis in long-range-transported saharan dust layers with airborne lidar. *Geophysical Research Letters*, *48*(18), e2021GL094418. https://doi.org/10.1029/2021gl094418

Heintzenberg, J. (2009). The samum-1 experiment over southern Morocco: Overview and introduction. *Tellus B: Chemical and Physical Meteorology*, *61*(1), 2–11. https://doi.org/10.3402/tellusb.v61i1.16791

Hinds, W. C. (1999). *Aerosol technology: Properties, behavior, and measurement of airborne particles*. John Wiley & Sons.

Huang, Y., Kok, J. F., Kandler, K., Lindqvist, H., Nousiainen, T., Sakai, T., et al. (2020). Climate models and remote sensing retrievals neglect substantial desert dust asphericity. *Geophysical Research Letters*, *47*(6), e2019GL086592. https://doi.org/10.1029/2019gl086592

IPCC. (2021). Climate change 2021: The physical science basis.

Jähn, M., Muñoz-Esparza, D., Chouza, F., Reitebuch, O., Knoth, O., Haarig, M., & Ansmann, A. (2016). Investigations of boundary layer structure, cloud characteristics and vertical mixing of aerosols at Barbados with large eddy simulations. *Atmospheric Chemistry and Physics*, *16*(2), 651–674. https://doi.org/10.5194/acp-16-651-2016

Jung, E., Albrecht, B., Prospero, J. M., Jonsson, H. H., & Kreidenweis, S. M. (2013). Vertical structure of aerosols, temperature, and moisture associated with an intense african dust event observed over the eastern caribbean. *Journal of Geophysical Research: Atmospheres*, *118*(10), 4623–4643. https://doi.org/10.1002/jgrd.50352

Kim, D., Chin, M., Yu, H., Diehl, T., Tan, Q., Kahn, R. A., et al. (2014). Sources, sinks, and transatlantic transport of North African dust aerosol: A multimodel analysis and comparison with remote sensing data. *Journal of Geophysical Research: Atmospheres*, *119*(10), 6259–6277. https://doi.org/10.1002/2013jd021099

Kind, R. (1992). One-dimensional aeolian suspension above beds of loose particles—A new concentration-profile equation. *Atmospheric Environment, Part A: General Topics*, *26*(5), 927–931. https://doi.org/10.1016/0960-1686(92)90250-o

Kok, J. F., Ridley, D. A., Zhou, Q., Miller, R. L., Zhao, C., Heald, C. L., et al. (2017). Smaller desert dust cooling effect estimated from analysis of dust size and abundance. *Nature Geoscience*, *10*(4), 274–278. https://doi.org/10.1038/ngeo2912

Mallios, S. A., Daskalopoulou, V., & Amiridis, V. (2022). Modeling of the electrical interaction between desert dust particles and the earth's atmosphere. *Journal of Aerosol Science*, *165*, 106044. https://doi.org/10.1016/j.jaerosci.2022.106044

Mallios, S. A., Drakaki, E., & Amiridis, V. (2020). Effects of dust particle sphericity and orientation on their gravitational settling in the earth's atmosphere. *Journal of Aerosol Science*, *150*, 105634. https://doi.org/10.1016/j.jaerosci.2020.105634

Maring, H., Savoie, D., Izaguirre, M., Custals, L., & Reid, J. (2003). Mineral dust aerosol size distribution change during atmospheric transport. *Journal of Geophysical Research*, *108*(D19), 8592. https://doi.org/10.1029/2002jd002536

McConnell, C., Highwood, E., Coe, H., Formenti, P., Anderson, B., Osborne, S., et al. (2008). Seasonal variations of the physical and optical characteristics of saharan dust: Results from the dust outflow and deposition to the ocean (dodo) experiment. *Journal of Geophysical Research*, *113*(D14), D14S05. https://doi.org/10.1029/2007jd009606

Middleton, N. J. (2017). Desert dust hazards: A global review. *Aeolian Research*, *24*, 53–63. https://doi.org/10.1016/j.aeolia.2016.12.001

Momen, M., Bou-Zeid, E., Parlange, M. B., & Giometto, M. (2018). Modulation of mean wind and turbulence in the atmospheric boundary layer by baroclinicity. *Journal of the Atmospheric Sciences*, *75*(11), 3797–3821. https://doi.org/10.1175/jas-d-18-0159.1

Muñoz, O., Volten, H., Hovenier, J., Nousiainen, T., Muinonen, K., Guirado, D., et al. (2007). Scattering matrix of large Saharan dust particles: Experiments and computations. *Journal of Geophysical Research*, *112*(D13). https://doi.org/10.1029/2006jd008074

Nicoll, K., Harrison, R., & Ulanowski, Z. (2010). Observations of Saharan dust layer electrification. *Environmental Research Letters*, *6*(1), 014001. https://doi.org/10.1088/1748-9326/6/1/014001

Otto, S., de Reus, M., Trautmann, T., Thomas, A., Wendisch, M., & Borrmann, S. (2007). Atmospheric radiative effects of an in situ measured saharan dust plume and the role of large particles. *Atmospheric Chemistry and Physics*, *7*(18), 4887–4903. https://doi.org/10.5194/acp-7-4887-2007

Pope, S. B. (2000). *Turbulent flows*. Cambridge university press.

Prandtl, L. (1952). *Essentials of fluid dynamics* (p. 452). blackie and son, ltd.

Rana, S., Anderson, W., & Day, M. (2021). An entrainment paradox: How hysteretic saltation and secondary transport augment atmospheric uptake of aeolian source materials. *Journal of Geophysical Research: Atmospheres*, *126*(10), e2020JD033493. https://doi.org/10.1029/2020jd033493

Reid, J. S., Kinney, J. E., Westphal, D. L., Holben, B. N., Welton, E. J., Tsay, S.-C., et al. (2003). Analysis of measurements of Saharan dust by airborne and ground-based remote sensing methods during the Puerto Rico dust experiment (pride). *Journal of Geophysical Research*, *108*(D19), 8586. https://doi.org/10.1029/2002jd002493

Richter, D., & Chamecki, M. (2018). Inertial effects on the vertical transport of suspended particles in a turbulent boundary layer. *Boundary-Layer Meteorology*, *167*(2), 235–256. https://doi.org/10.1007/s10546-017-0325-3

Ridley, D., Heald, C., & Ford, B. (2012). North African dust export and deposition: A satellite and model perspective. *Journal of Geophysical Research*, *117*(D2). https://doi.org/10.1029/2011jd016794

Rittmeister, F., Ansmann, A., Engelmann, R., Skupin, A., Baars, H., Kanitz, T., & Kinne, S. (2017). Profiling of Saharan dust from the Caribbean to Western Africa–Part 1: Layering structures and optical properties from shipborne polarization/Raman lidar observations. *Atmospheric Chemistry and Physics*, *17*(21), 12963–12983. https://doi.org/10.5194/acp-17-12963-2017

Ruiz, J. (1996). The role of turbulence in the sedimentation loss of pelagic aggregates from the mixed layer. *Journal of Marine Research*, *54*(2), 385–406. https://doi.org/10.1357/0022240963213367

Ryder, C. (2021). Radiative effects of increased water vapor in the upper Saharan air layer associated with enhanced dustiness. *Journal of Geophysical Research: Atmospheres*, *126*(21), e2021JD034696. https://doi.org/10.1029/2021jd034696

Shao, Y. (2008). *Physics and modeling of wind erosion* (2nd ed.). Springer.

Siebert, H., Beals, M., Bethke, J., Bierwirth, E., Conrath, T., Dieckmann, K., et al. (2013). The fine-scale structure of the trade wind cumuli over Barbados–an introduction to the carriba project. *Atmospheric Chemistry and Physics*, *13*(19), 10061–10077. https://doi.org/10.5194/acp-13-10061-2013

Tanré, D., Haywood, J., Pelon, J., Léon, J., Chatenet, B., Formenti, P., & Myhre, G. (2003). Measurement and modeling of the saharan dust radiative impact: Overview of the Saharan dust experiment (shade). *Journal of Geophysical Research*, *108*(D18), 8574. https://doi.org/10.1029/2002jd003273

Toth, J. R.,III, Rajupet, S., Squire, H., Volbers, B., Zhou, J., Xie, L., et al. (2020). Electrostatic forces alter particle size distributions in atmospheric dust. *Atmospheric Chemistry and Physics*, *20*(5), 3181–3190. https://doi.org/10.5194/acp-20-3181-2020

Tsigaridis, K., Krol, M., Dentener, F., Balkanski, Y., Lathiere, J., Metzger, S., et al. (2006). Change in global aerosol composition since preindustrial times. *Atmospheric Chemistry and Physics*, *6*(12), 5143–5162. https://doi.org/10.5194/acp-6-5143-2006

Twohy, C. H., Kreidenweis, S. M., Eidhammer, T., Browell, E. V., Heymsfield, A. J., Bansemer, A. R., et al. (2009). Saharan dust particles nucleate droplets in eastern Atlantic clouds. *Geophysical Research Letters*, *36*(1), L01807. https://doi.org/10.1029/2008gl035846

Van Der Does, M., Knippertz, P., Zschenderlein, P., Giles Harrison, R., & Stuut, J.-B. W. (2018). The mysterious long-range transport of giant mineral dust particles. *Science Advances*, *4*(12), eaau2768. https://doi.org/10.1126/sciadv.aau2768

Weinzierl, B., Ansmann, A., Prospero, J., Althausen, D., Benker, N., Chouza, F., et al. (2017). The Saharan aerosol long-range transport and aerosol-cloud-interaction experiment: Overview and selected highlights. *Bulletin of the American Meteorological Society*, *98*(7), 1427–1451. https://doi.org/10.1175/bams-d-15-00142.1

Westbrook, C. (2008). The fall speeds of sub-100 $\mu$m ice crystals. *Quarterly Journal of the Royal Meteorological Society*, *134*(634), 1243–1251. https://doi.org/10.1002/qj.290

Wurzler, S., Reisin, T. G., & Levin, Z. (2000). Modification of mineral dust particles by cloud processing and subsequent effects on drop size distributions. *Journal of Geophysical Research*, *105*(D4), 4501–4512. https://doi.org/10.1029/1999jd900980

Wygnanski, I., & Fiedler, H. E. (1970). The two-dimensional mixing region. *Journal of Fluid Mechanics*, *41*(2), 327–361. https://doi.org/10.1017/s0022112070000630

Yu, H., Chin, M., Yuan, T., Bian, H., Remer, L. A., Prospero, J. M., et al. (2015). The fertilizing role of African dust in the amazon rainforest: A first multiyear assessment based on data from cloud-aerosol lidar and infrared pathfinder satellite observations. *Geophysical Research Letters*, *42*(6), 1984–1991. https://doi.org/10.1002/2015gl063040

## References From the Supporting Information

Raupach, M. R., Finnigan, J. J., & Brunet, Y. (1996). Coherent eddies and turbulence in vegetation canopies: The mixing-layer analogy. In *Boundary-Layer Meteorology 25th Anniversary Volume, 1970–1995* (pp. 351–382). Springer.

Rodakoviski, R., Kok, J., & Chamecki, M. (2023). Data from: Dust settling from turbulent layers in the free troposphere: Implications for the Saharan air layer [Dataset]. Dryad. https://doi.org/10.5068/D11D5D

Rogers, M. M., & Moser, R. D. (1994). Direct simulation of a self-similar turbulent mixing layer. *Physics of Fluids*, *6*(2), 903–923. https://doi.org/10.1063/1.868325

Seinfeld, J., & Pandis, S. (2016). *Atmospheric chemistry and physics* (3rd ed.). Wiley.